

conductivity measurements could be grown.

The band electronic structure<sup>15</sup> calculated for a layer of (ET<sup>+</sup>)<sub>2</sub> dimers is shown in Figure 4. In each (ET<sup>+</sup>)<sub>2</sub> dimer, the HOMO's of the ET<sup>+</sup> cations interact to give the bonding and antibonding levels  $\psi_+$  and  $\psi_-$ , respectively. The lower and upper bands are largely described by the bonding and antibonding combinations of the HOMO's in each (ET<sup>+</sup>)<sub>2</sub> dimer, respectively. These two bands are slightly dispersive along the *a* direction but almost dispersionless along the *b* direction. This reflects the fact that short interdimer S...S contacts of less than 3.60 Å occur only along the *a* direction. With the formal oxidation state of ET<sup>+</sup>, only the lower band is filled if a low-spin band filling is adopted, as indicated by the diamagnetic properties (vide supra). This leads to a band gap of 0.42 eV, and (ET)BiI<sub>4</sub> is expected to be a semiconductor with high activation energy.

## Discussion

The original intent of our work was to obtain a 2:1 salt of ET with a very large polarizable, "tetrahedral" anion BiI<sub>4</sub><sup>-</sup>, and hence with soft C—H...I contacts between the donor molecules and the anions. This attempt led to an unexpected 1:1 salt (ET)BiI<sub>4</sub> that contains polymeric anions, i.e., [BiI<sub>4</sub><sup>-</sup>]<sub>∞</sub> chains. As is often the case, this result may reflect the fact that the [BiI<sub>4</sub><sup>-</sup>]<sub>∞</sub> anions are too large to allow formation of a 2:1 salt with ET. Soft C—H...anion contacts are expected from a large, polarizable anion, but such an anion may prevent the formation of a 2:1 salt. Thus, a balance of polarizability and size appears to be crucial in obtaining a 2:1 salt with soft C—H...anion contacts.

The packing motif for the ET donor molecule network in (ET)BiI<sub>4</sub> is novel and does not resemble that of any other ET salt. Due to the unavailability of sufficiently large crystals, the electrical conductivity of (ET)BiI<sub>4</sub> has not yet been measured directly, but the ESR measurements (i.e., lack of an *intrinsic* signal) and band electronic structure calculations indicate that the compound is a semiconductor or insulator. When the electronic structure of an (ET<sup>+</sup>)<sub>2</sub> dimer is described by the configuration ( $\psi_+$ )<sup>2</sup> (ignoring the weaker *interdimer* interactions), (ET)BiI<sub>4</sub> would be diamagnetic in the absence of impurities. If the electronic structure of (ET<sup>+</sup>)<sub>2</sub> were described by the configuration ( $\psi_+$ )( $\psi_-$ ), as appropriate when the intermolecular interaction in each (ET<sup>+</sup>)<sub>2</sub> dimer

(15) Details of our tight-binding band electronic structure calculations are described in: Whangbo, M.-H.; Williams, J. M.; Leung, P. C. W.; Beno, M. A.; Emge, T. J.; Wang, H. H.; Carlson, K. D.; Crabtree, G. W. *J. Am. Chem. Soc.* **1985**, *107*, 5815.

is weak, the singlet and triplet states of each dimer would have a small energy difference, thereby giving rise to an ESR signal from the thermally populated triplet state. However, the observed ESR signal is so weak as to rule out that possibility, and the electronic structure of (BEDT-TTF)BiI<sub>4</sub> is best described as composed of strongly antiferromagnetically coupled dimers.

(ET)BiI<sub>4</sub> is an example of an ET salt with polymeric counteranions. The latter include not only the superconductors  $\kappa$ -(ET)<sub>2</sub>Cu(SCN)<sub>2</sub><sup>16</sup> and (ET)<sub>4</sub>Hg<sub>3-x</sub>X<sub>3</sub> (X = Cl, Br)<sup>17,18</sup> but also the nonsuperconducting salts (ET)Ag<sub>4</sub>(CN)<sub>5</sub>,<sup>19</sup> (ET)<sub>3</sub>Ag<sub>6.4</sub>I<sub>8</sub>,<sup>20</sup>  $\kappa$ -(ET)<sub>2</sub>Ag(CN)<sub>2</sub>(H<sub>2</sub>O),<sup>21</sup> (ET)Ag<sub>1.6</sub>(SCN)<sub>2</sub>,<sup>22</sup> (ET)Ag<sub>2.4</sub>Br<sub>3</sub>,<sup>23</sup> (ET)Cu<sub>2</sub>(NCS)<sub>3</sub>,<sup>22</sup> (ET)<sub>2</sub>Cu<sub>5</sub>I<sub>6</sub>,<sup>24</sup> and (ET)<sub>2</sub>HgBr<sub>3</sub>(TCE).<sup>25</sup>

**Acknowledgment.** Work at Argonne National Laboratory and at North Carolina State University was sponsored by the U.S. Department of Energy, Office of Basic Energy Sciences, Division of Materials Sciences, under Contract W-31-109-ENG-38 and Grant DE-FG-05-86ER45259, respectively. S.M.B. and M.J.L. are Student Undergraduate Research Participants from St. Xavier College, Chicago, IL, and Centre College, Danville, KY, respectively, sponsored by the Argonne Division of Educational Programs. We wish to thank both reviewers for their extremely helpful comments regarding the ESR results.

**Supplementary Material Available:** Tables of details of X-ray diffraction data collection and anisotropic thermal parameters (2 pages); a listing of structure factor amplitudes (11 pages). Ordering information is given on any current masthead page.

- (16) Urayama, H.; Yamochi, H.; Saito, G.; Sato, S.; Kawamoto, A.; Tanaka, J.; Mori, T.; Maruyama, Y.; Inokuchi, H. *Chem. Lett.* **1988**, 463.
- (17) Shibaeva, R. P.; Rozenberg, L. P. *Kristallografiya* **1988**, *33*, 1402.
- (18) Lyubovskaya, R. N.; Zhilyaeva, E. I.; Pesotskii, S. I.; Lyubovskii, R. B.; Atovmyan, L. O.; D'yachenko, O. A.; Takhirov, T. G. *Pis'ma Zh. Eksp. Teor. Fiz.* **1987**, *46*, 149; *JETP Lett. (Engl. Transl.)* **1987**, *46*, 188.
- (19) Geiser, U.; Wang, H. H.; Gerdorn, L. E.; Firestone, M. A.; Sowa, L. M.; Williams, J. M.; Whangbo, M.-H. *J. Am. Chem. Soc.* **1985**, *107*, 8305.
- (20) Geiser, U.; Wang, H. H.; Donega, K. M.; Anderson, B. A.; Williams, J. M.; Kwak, J. F. *Inorg. Chem.* **1986**, *25*, 401.
- (21) Kurmoo, M.; Talham, D. R.; Pritchard, K. L.; Day, P.; Stringer, A. M.; Howard, J. A. K. *Synth. Met.* **1988**, *27*, A177.
- (22) Geiser, U.; Beno, M. A.; Kini, A. M.; Wang, H. H.; Schultz, A. J.; Gates, B. D.; Cariss, C. S.; Carlson, K. D.; Williams, J. M. *Synth. Met.* **1988**, *27*, A235.
- (23) Geiser, U.; Wang, H. H.; Rust, P. R.; Tonge, L. M.; Williams, J. M. *Mol. Cryst. Liq. Cryst.* **1990**, *181*, 117.
- (24) Shibaeva, R. P.; Lobkovskaya, R. M. *Kristallografiya* **1988**, *33*, 408; *Sov. Phys.—Crystallogr. (Engl. Transl.)* **1988**, *33*, 241.
- (25) Geiser, U.; Wang, H. H.; Kleinjan, S. B.; Williams, J. M.; Whangbo, M.-H. To be published.

Contribution from the Research School of Chemistry, Australian National University, Canberra, ACT 2601, Australia, and Department of Physics, Faculty of Science, Chiba University, Chiba 260, Japan

## Optical Spectrum of K<sub>2</sub>CuF<sub>4</sub>

Mark J. Riley,<sup>†</sup> Lucjan Dubicki,<sup>\*†</sup> Grainne Moran,<sup>†</sup> Elmars R. Krausz,<sup>†</sup> and Isao Yamada<sup>‡</sup>

Received July 11, 1989

The absorption, magnetic circular dichroism (MCD), and Zeeman spectra of K<sub>2</sub>CuF<sub>4</sub> single crystals were measured below 5 K. An unambiguous assignment of the d-d transitions can be made from the experimental spectra. Two zero-phonon magnetic dipole origins were observed, and their energies, intensities, polarization properties, and MCD parameters agree with those given by a ligand field model for a tetragonally elongated complex. The extensive vibrational fine structure on one of the transitions has been partially analyzed. An electric dipole vibronic origin must be interpreted on the basis of a D<sub>4h</sub> factor group rather than the D<sub>2h</sub> site symmetry of the CuF<sub>6</sub><sup>4-</sup> chromophore.

## Introduction

Although copper(II) complexes display a wide variety of coordinations and geometries, there are to date only a few known

examples of a pure copper(II) compound with a compressed octahedral geometry.<sup>1</sup> Until recently, K<sub>2</sub>CuF<sub>4</sub> was also often cited as having a compressed geometry.<sup>2</sup> This prompted magnetic<sup>3</sup>

\* Address correspondence to this author.

<sup>†</sup> Australian National University.

<sup>‡</sup> Chiba University.

(1) (a) Reinen, D. *Comments Inorg. Chem.* **1983**, *2*, 227. (b) Wingefeld, G.; Hoppe, R. Z. *Anorg. Allg. Chem.* **1984**, *516*, 223. (c) Effenberger, H. Z. *Kristallogr.* **1989**, *188*, 43.

and EPR<sup>4</sup> studies which suggested that there was a cooperative ordering of elongated  $CuF_6^{4-}$  octahedra within the (001) plane, which was later confirmed by more accurate crystal structures.<sup>5-8</sup>

More recently, this compound has been subject to numerous detailed magneto-optical studies,<sup>9-16</sup> in which the assignment of the electronic excited states is at variance with that expected by simple ligand field arguments. On the one hand, the exhaustive studies of Kleemann and co-workers<sup>10-13</sup> have used high-resolution absorption, magnetic circular, and linear dichroism spectra of single crystals to support their assignment of the near-IR bands to the components of the  ${}^2E_g \rightarrow {}^2T_{2g}$  transition of the parent octahedral complex, in a seemingly definitive manner. Alternatively, the assignments in the work of Reinen et al.<sup>4,7</sup> were based on low-resolution powder spectra together with the "chemical intuition" gained from the study of the bonding characteristics of this and other copper(II) fluorides. The latter attributed one of the observed bands to the  $(x^2 - y^2) \rightarrow (z^2)$  transition between the split components of the  ${}^2E_g$  octahedral state.

In the present work the MCD, Zeeman, and absorption spectra of single crystals of  $K_2CuF_4$  have been reexamined in an attempt to resolve this controversy. The present assignment of these near-infrared transitions agrees with that of Reinen et al.<sup>4,7</sup> Such an assignment is shown to be that expected from the energies and intensities of the magnetic dipole origins calculated from ligand field theory. An additional sharp magnetic dipole origin, which has not been previously observed, has been found at an energy that makes the assignment of Kleemann et al.<sup>10-13</sup> untenable. A sharp vibronic origin requires an interpretation in terms of the factor group symmetry of the unit cell, rather than the "isolated molecule" approach of previous studies. This is one of the few cases where such an approach has been required in the optical spectroscopy of inorganic compounds.

## Experimental Section

**Sample Preparation.** Large transparent pale blue crystals of good optical quality were grown by a method described previously.<sup>16</sup> The large plates (typically  $8 \times 8$  mm) were usually produced with faces parallel to the (001) cleavage plane. Smaller crystals ( $3 \times 1.5$  mm) with faces parallel to the (100) plane were obtained by mechanically cleaving and polishing the large plates. Typical thicknesses of the crystals were 0.3–1.0 mm.

**Instrumentation.** Preliminary absorption measurements over the range  $5000\text{--}40000\text{ cm}^{-1}$  were performed on a Cary 17 spectrometer with the sample held in a Helium flow tube. The axial absorption spectrum over the range  $500\text{--}5000\text{ cm}^{-1}$  at  $\sim 100\text{ K}$  was measured on a Perkin-Elmer PE1800/PE7500 FT-IR spectrometer. Absorption and MCD measurements down to 1.6 K were made on an apparatus described previously.<sup>17,18</sup>

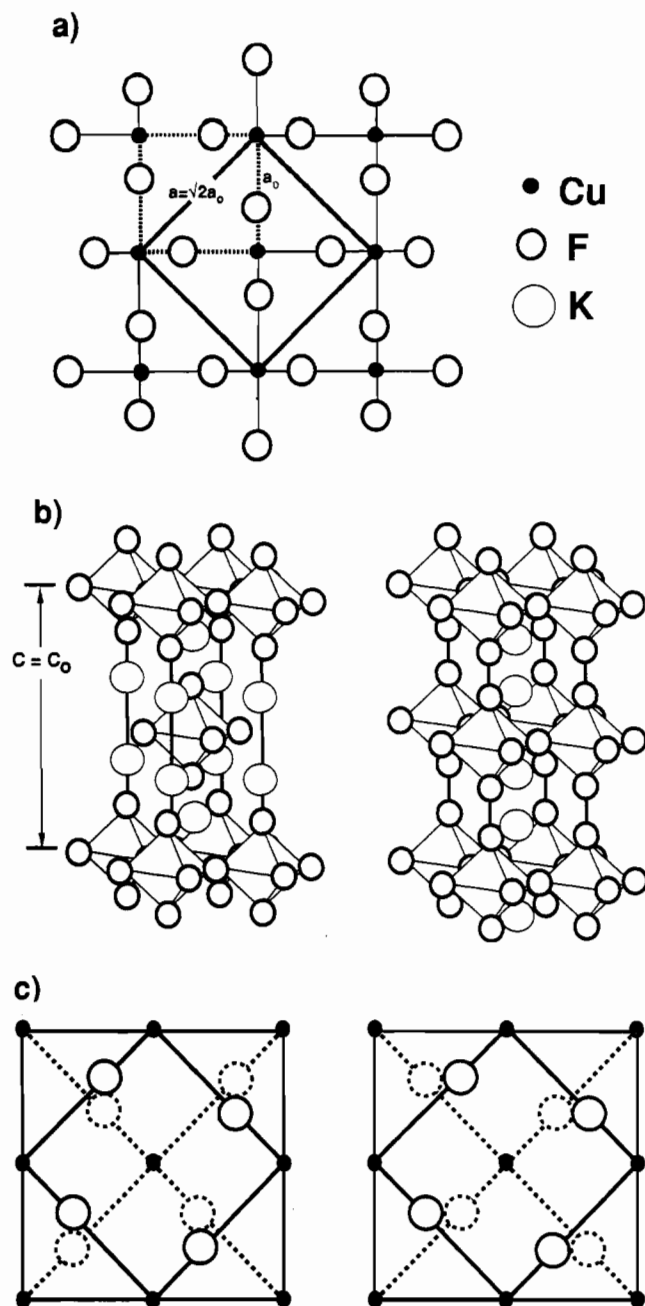


**Figure 1.** Distortions of  $K_2CuF_4$  away from the ideal perovskite structure: (a) cooperative ordering of the elongated octahedra in the  $z = 0$  plane; (b) the order/disorder of the (001) slide planes (the ordered  $K_2NiF_4$  type structure shown on the left-hand side and the disordered structure shown on the right-hand side); (c) the two kinds of domain structure (the dotted and solid lines represent the  $z = 0$  and  $z = 1/2$  levels, respectively). The unit cell dimensions of the  $K_2NiF_4$  parent structure are  $a_0$  and  $c_0$ .

- (2) (a) Cotton, F. A.; Wilkinson, G. *Advanced Inorganic Chemistry*, 3rd ed.; Interscience: New York, 1972; p 912. (b) Greenwood, N. N.; Earnshaw, A. *Chemistry of the Elements*; Pergamon Press: New York 1984; p 1382. (c) Knox, K. *J. Chem. Phys.* **1959**, *30*, 991.
- (3) Khomskii, D. I.; Kugel, K. I. *Solid State Commun.* **1973**, *13*, 763.
- (4) Friebel, C.; Reinen, D. *Z. Anorg. Allg. Chem.* **1974**, *407*, 193.
- (5) Haegeler, R.; Babel, D. *Z. Anorg. Allg. Chem.* **1974**, *409*, 11.
- (6) Herdtweck, E.; Babel, D. *Z. Anorg. Allg. Chem.* **1981**, *474*, 113.
- (7) Reinen, D.; Krause, S. *Inorg. Chem.* **1981**, *20*, 2750.
- (8) Hidaka, M.; Inoue, K.; Yamada, I.; Walker, P. J. *Physica* **1983**, *121B*, 343.
- (9) Laiho, R. *Phys. Status Solidi B* **1975**, *69*, 579.
- (10) Kleemann, W.; Farge, Y. *J. Phys. Lett.* **1974**, *35*, L135.
- (11) Kleemann, W.; Farge, Y. *J. Phys.* **1975**, *36*, 1293.
- (12) Ferré, J.; Regis, M.; Farge, Y.; Kleemann, W. *Physica* **1977**, *89B*, 181.
- (13) Ferré, J.; Regis, M.; Farge, Y.; Kleemann, W. *J. Phys. C* **1979**, *12*, 2671.
- (14) Kaneko, M.; Kuwabara, G.; Misu, A. *Solid State Commun.* **1976**, *18*, 1085.
- (15) Natsume, Y.; Yamada, I. *J. Phys. Soc. Jpn.* **1985**, *54*, 4410.
- (16) Yamada, I. *J. Phys. Soc. Jpn.* **1972**, *33*, 979.
- (17) Krausz, E. R.; Ludi, A. *Inorg. Chem.* **1985**, *24*, 939.
- (18) Krausz, E. R.; Mau, A. W. H. *Inorg. Chem.* **1986**, *25*, 1484.

Briefly, light from a 150-W tungsten lamp was dispersed by a Spex 1704 monochromator fitted with either a 1.6- or 1.0- $\mu\text{m}$  grating. The light beam was then chopped at 800 Hz and circularly polarized by a photoelastic stress modulator, passed through the sample held in an Oxford Instruments SM4 cryostat with a 5 T superconducting magnet, and then focused onto a liquid-nitrogen-cooled InSb detector. Both the totally transmitted and differential circularly polarized light were measured by using two PAR 124A lockin amplifiers and accumulated simultaneously on a computer.

Wavelength calibration was carried out with a mercury lamp,<sup>19</sup> and the spectra were found to be reproducible to within  $\pm 2\text{ cm}^{-1}$  for the sharpest lines. The circular dichroism was calibrated both with a standard nickel tartrate solution and a sapphire quarter-wave plate with a polarizer.<sup>20</sup> This last step is important because it is only for small

(19) Weast, R. C. *CRC Handbook of Chemistry and Physics*, 6th ed.; CRC Press: Boca Raton, FL, 1987; p E-257.

values of  $\Delta A$  ( $=A_L - A_R$ ) that there is a linear relationship between the ratio of the difference and the sum of the left and right circularly polarized transmitted light,  $(I_L - I_R)/(I_L + I_R)$ . For spectra with large  $\Delta A$ , the explicit logarithmic function must be used in converting transmitted to absorbed quantities rather than assuming the above relationship. The use of the  $\lambda/4$  sapphire plate, which gives totally left and right circularly polarized light over the entire spectral range of interest, checks the correctness of such a calibration. It should be noted that the sign convention of  $\Delta A$  adopted in refs 9–13 is opposite to the standard convention<sup>21</sup> used in this work.

### $K_2CuF_4$ Crystal and Magnetic Structure

$K_2CuF_4$  has the basic perovskite-type layer structure of  $K_2NiF_4$  with three types of deviations from this ideal structure. These are shown in Figure 1 as (a) a distortion of the  $CuF_6^{4-}$  octahedra within the (001) planes, (b) a stacking order/disorder of the  $CuF_6^{4-}$  octahedra between planes, and (c) the direction of the distorted  $CuF_6^{4-}$  octahedra relative to those in adjacent planes. Compounds of this type have assumed a special interest with the recent discovery of high-temperature superconductors, some of which appear to be related to flawed perovskite-type layer structures.<sup>22</sup>

The distortion within the (001) plane is due to a strong static Jahn–Teller deformation of the  $CuF_6^{4-}$  octahedra. The cooperative “antiferrodistortive” order of these predominantly elongated octahedra is shown in Figure 1a, where the enlarged unit cell dimensions in the (001) plane are related to those of the parent  $K_2NiF_4$  structure through the relation  $a = \sqrt{2}a_0$ .

The stacking of the corner sharing octahedra can be either “ordered” or “disordered”, as shown in Figure 1b. It has been suggested that this “wrong” stacking of the  $c$  planes can cause both the ordered and disordered structures to coexist in the same sample.<sup>8</sup> A careful study by Hidaka et al.<sup>8</sup> on a perfectly ordered single crystal revealed a multidomain structure where a single domain has the orthorhombic space group  $D_{2h}^{18}$ . The size of the unit cell is  $\sqrt{2}a_0 \times \sqrt{2}b_0 \times c_0$  ( $a_0 = b_0$ ), where  $a_0 \times a_0 \times c_0$  is the unit cell of the parent  $K_2NiF_4$  structure.

There are two types of domains that result from the two different ways that the in-plane  $F^-$  ions are displaced from the  $Cu^{2+}$  ion relative to those of an adjacent plane, as illustrated in Figure 1c. In the studies of Babel and co-workers,<sup>5,6</sup> the crystal structure of  $K_2CuF_4$  has been interpreted with a disorder along the  $c$  axis, although it has since been shown that it is possible to obtain ordered crystals with a single-domain structure.<sup>23</sup> As the orthorhombic symmetry of the  $D_{2h}^{18}$  space group for a single domain comes only from this stacking condition of the layers, Hidaka et al.<sup>8</sup> found that  $a = b$  for an ordered single-domain crystal.

Following Kaneko et al.,<sup>14</sup> we assume that the interlayer effects shown in Figure 1b,c have a negligible effect on the optical spectrum, and hence the effective space group for  $K_2CuF_4$  will be  $D_{4h}^5$ . This is a reasonable assumption since the electronic transitions are localized mainly on a single  $Cu^{2+}$  ion. Phonons involving the relative motions of the layers are not expected to be strongly coupled to localized electronic transitions, although it will be shown that the concerted motions of the  $CuF_6^{4-}$  octahedra within the layer do play an important role. It should be noted that recent work<sup>23</sup> has detected the effects of interlayer coupling in the Raman spectrum of  $K_2CuF_4$ , which required the orthorhombic  $D_{2h}^{18}$  space group for a complete analysis.

In the  $D_{4h}^5$  space group, the  $Cu^{2+}$  ions occupy  $D_{2h}$  sites (Wyckoff position 2d). The local molecular axes of the two ions per unit cell are defined in Figure 2 such that the right-handed  $x, y, z$  axes correspond to the short, medium, and long bonds, respectively. The short and long bonds involve bridging fluoride ions, while the medium bonds lie parallel to the  $c$  axis and involve terminal fluoride ions. The two  $Cu^{2+}$  sites of the unit cell are related by

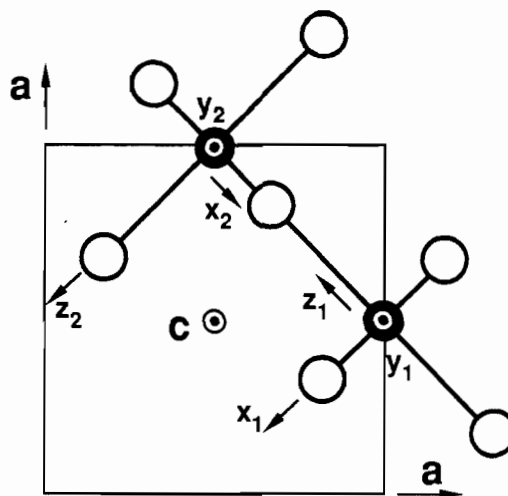


**Figure 2.** Relation between the molecular axes and the crystal axes used in the text. The  $x, y,$  and  $z$  axes correspond to the short, medium, and long bonds, respectively. The two  $Cu^{2+}$  sites are related by a  $C_4$  operation about the out-of-plane axis shown as  $\odot$ .

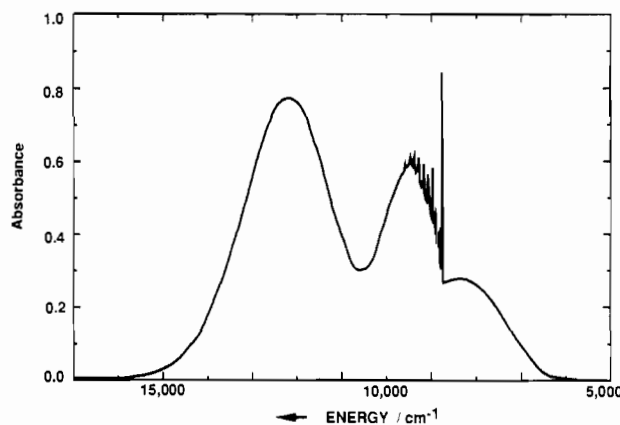


**Figure 3.** Absorption spectrum of  $K_2CuF_4$  for light propagated parallel to the  $c$  axis at 5 K. The crystal is  $\sim 0.25$  mm thick.

a  $C_4$  operation about the  $c$  axis. The orthorhombic distortion of the tetragonally elongated octahedra is small, the reported bond lengths in picometers being 190.9, 193.9, and 223.8,<sup>6</sup> 186.3, 194.9, and 227.6,<sup>7</sup> and, in the most recent data, 193.2, 193.9, and 222.2.<sup>8</sup> The main features of the present work can be explained by assuming a local  $D_{4h}$  environment of the  $CuF_6^{4-}$  octahedra.

The orthogonal alignment of the long Cu–F bonds within the (001) plane results in a ferromagnetic coupling between the  $Cu^{2+}$  ions.  $K_2CuF_4$  is an excellent example of a two-dimensional Heisenberg ferromagnet with  $J/k_B \sim +10$  K, where  $\mathcal{H}_{ex} = -2J \sum_{ij} S_i \cdot S_j$ .<sup>16</sup>

A small interplanar exchange interaction,  $J' \sim 6.6 \times 10^{-4}$  J, is believed to be responsible for the onset of three-dimensional order below  $T_c = 6.25$  K. A small anisotropy in the in-plane exchange interactions fixes the direction of spontaneous magnetization along the crystal  $a$  axes<sup>24</sup> (Figure 1a) and leads to four types of ferromagnetic domains.

Simple molecular field theory<sup>25</sup> gives an internal exchange field of  $B_{ex} \sim 30$  T, where  $2\mu_B B_{ex} \sim z(-2J)\langle S \rangle$ ,  $z = 4$ , and  $\langle S \rangle = 1/2$ . The internal field can be rotated within the (001) easy plane and along the hard  $c$  axis by applying external magnetic fields of  $\sim 0.1$  and 0.5 T, respectively, thereby transforming the multidomains into a single magnetic domain with  $B_{ex}$  parallel to  $B_{appl}$ .<sup>11</sup> All our magneto-optical experiments were carried out under the condition of ferromagnetic saturation with an applied field of 5 T.

(20) Osborne, G. A.; Cheng, J. C.; Stephens, P. J. *Rev. Sci. Instrum.* **1973**, *44*, 10.

(21) Piepho, S. B.; Schatz, P. N. *Group Theory in Spectroscopy with Applications to Magnetic Circular Dichroism*; Wiley: New York, 1983; Appendix A.

(22) Hazen, R. M. *Sci. Am.* **1988**, *258* (June), 52.

(23) Totani, M.; Fukada, Y.; Itoh, M.; Yamada, I. *Phys. Rev. B* **1989**, *40*, 10577.

(24) Kleemann, W.; Schäfer, F. J. *J. Magn. Magn. Mater.* **1980**, *21*, 143.

(25) Smart, J. S. *Effective Field Theories of Magnetism*; W. B. Saunders: Philadelphia, PA, 1966.

**Table I.** Spectroscopic Data for  $K_2CuF_4$ 

energy, <sup>a</sup> cm <sup>-1</sup>	half-width, <sup>b</sup> cm <sup>-1</sup>	polarization <sup>c</sup>			$\Delta A/A$
		$\alpha$	$\sigma$	$\pi$	
Broad Bands					
8330	2400	1	0.98	0.86	
9420	1600	1	0.85	1.06	
12140	2500	1	1.03	0.54	
Zero-Phonon Lines					
8764	3.6	1	0.14	1.08	-0.28
10214 <sup>d</sup>	~4	1	1.65	0.93	+0.8
Vibronic Origin					
8977	~4	1	0.97	0.13	0

<sup>a</sup>The uncertainty in the energies is  $\pm 10$  cm<sup>-1</sup> for the broad bands and  $\pm 2$  cm<sup>-1</sup> for the sharp lines. <sup>b</sup>Half-width = full width at half-height. <sup>c</sup>The intensities are normalized with respect to the  $\alpha$  polarization. The estimated error is  $\pm 0.05$  due to the uncertainty in the crystal thickness. <sup>d</sup>Measured in  $\alpha$  polarization with an applied axial field of 5 T (see Figure 6).

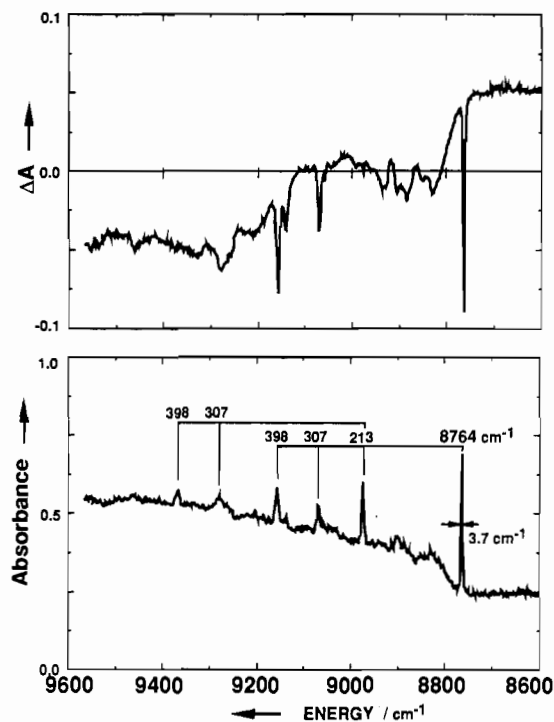


**Figure 4.** MCD and axial absorption spectra of the vibrational fine structure near 9000 cm<sup>-1</sup> at 1.8 K. The light direction and an applied magnetic field of 5 T are parallel to the *c* axis in both cases.

## Results

The polarization of the incident light propagating in the *k* direction, with respect to the crystal axes, is related to the molecular geometry of the two copper sites by

$$\begin{aligned} \alpha(k \parallel c, E \perp c, H \perp c) &= D_x + D_z + M_x + M_z \\ \sigma(k \perp c, E \perp c, H \parallel c) &= D_x + D_z + 2M_y \\ \pi(k \perp c, E \parallel c, H \perp c) &= 2D_y + M_x + M_z \end{aligned} \quad (1)$$

Here  $D_i$  ( $M_i$ ) is the dipole strength for an electric (magnetic) vector of the incident light parallel to the *i*th molecular direction in Figure 2.

The axial ( $\alpha$ ) absorption spectrum is shown in Figure 3. No other absorption was detected to lower energy until  $\sim 800$  cm<sup>-1</sup> and to higher energy until  $\sim 20\,000$  cm<sup>-1</sup>, where a broad weak absorption assigned as a double excitation<sup>13</sup> was observed. The temperature dependence of the spectrum was found to be consistent with a vibronic mechanism for the bulk of the observed intensity, as expected from an ion at a centrosymmetric site and in agreement with previous studies.<sup>9,11</sup> Although the overlapping

**Table II.** Analysis of the Vibrational Fine Structure of the Electronic Transition Near 9000 cm<sup>-1</sup>

energy, cm <sup>-1</sup>	assgt <sup>a</sup>	ground-state freq, cm <sup>-1</sup>
8764 + 0	0-0 magnetic dipole origin	
67		
88		
136		
173		
213	$\nu_{a_{2u}^2}$	$\sim 230^b$
285		
307	$\nu_{a_{1g}^2}$	318 <sup>c</sup>
398	$\nu_{a_{1g}^1}$	403 <sup>c</sup>
441		
520	$\nu_{a_{2u}^2} + \nu_{a_{1g}^2}$	
610	$\nu_{a_{2u}^2} + \nu_{a_{1g}^1}$	
703	$\nu_{a_{1g}^1} + \nu_{a_{1g}^2}$	

<sup>a</sup>The vibrational species are denoted by their symmetry labels as given in Appendix A2. A superscript distinguishes vibrations of the same irreducible representation in order of decreasing energy following ref 15. <sup>b</sup>Observed for  $K_2MnF_4$ ; see text. <sup>c</sup>Reference 15.

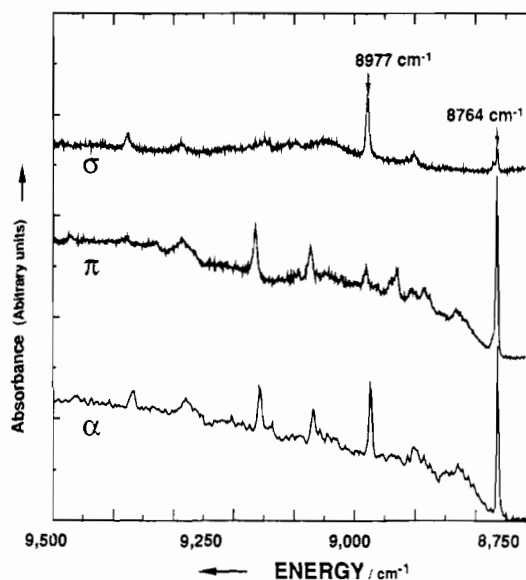


**Figure 5.** Polarization properties of the zero-phonon (8764 cm<sup>-1</sup>) and vibronic (8977 cm<sup>-1</sup>) origins at 2 K. The  $\alpha$  and  $\sigma/\pi$  spectra were measured on crystals  $\sim 0.25$  and  $\sim 1.1$  mm thick, respectively. The spectra have been scaled to give their correct relative intensities.

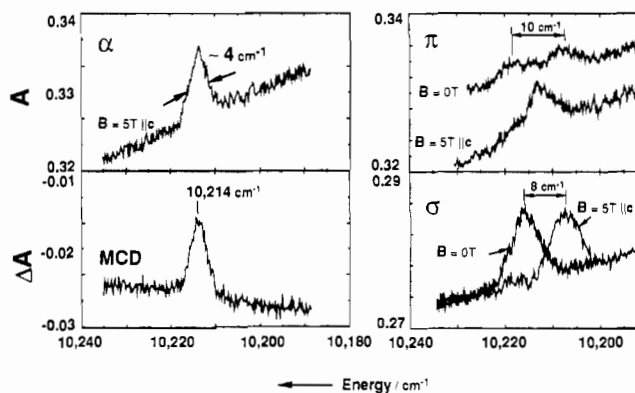


**Figure 6.** MCD (5 T) and Zeeman spectra of the high-energy magnetic dipole origin at 1.6 K. The spectra resolution is  $\sim 2$  cm<sup>-1</sup>. Note that the splitting in the  $\pi$  spectrum in zero-applied magnetic field is quenched for  $B = 5$  T ( $\parallel c$ ).

bands preclude a detailed study, the overall temperature dependence can be readily fitted to a simple coth law.<sup>9,11</sup> This, together with the fact that only a small red shift is observed, implies that both the ground- and excited-state potential surfaces are relatively harmonic<sup>26</sup> and will justify some of the approximations used later

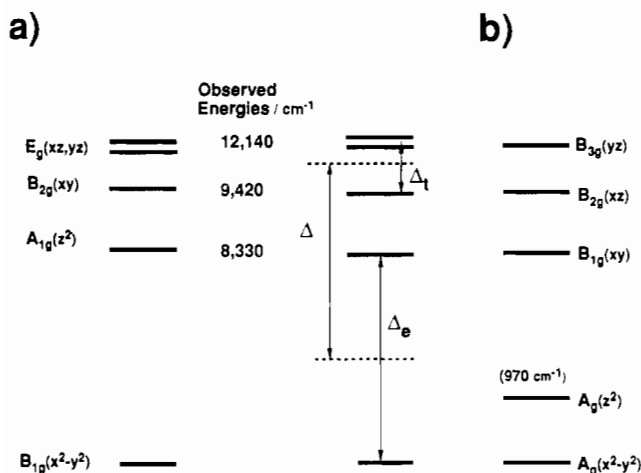


**Figure 7.** Assignment of the d-d transitions shown in Figures 3–6: (a) present work, based on local  $D_{4h}$  symmetry; (b) the assignment of Kleemann et al.,<sup>10–13</sup> based on local  $D_{2h}$  symmetry. The energies of the Franck–Condon maxima are shown to the right of the energy levels. The AOM parameters derived with (2) and (3) are for assignment a  $\sigma_{\perp} = 5630 \text{ cm}^{-1}$ ,  $\sigma_{\parallel} = 1470 \text{ cm}^{-1}$ ,  $\pi_{\perp} = 1880 \text{ cm}^{-1}$ ,  $\pi_{\parallel} = 490 \text{ cm}^{-1}$  and for assignment b  $\sigma_{\perp}$  (average) =  $-1130 \text{ cm}^{-1}$ ,  $\sigma_{\parallel} = -1620 \text{ cm}^{-1}$ ,  $\pi_{\perp}$  (average) =  $-2830 \text{ cm}^{-1}$ ,  $\pi_{\parallel} = -4040 \text{ cm}^{-1}$ .

in determining approximate potential energy surfaces from the spectra. The Franck–Condon maxima, half-widths, and polarization properties of the observed absorption bands are given in Table I.

The extensive vibrational fine structure of the band near  $9000 \text{ cm}^{-1}$  is shown in more detail in Figure 4 together with the MCD spectrum. The observed energies and a partial vibrational analysis of the structure are given in Table II. The polarization properties of the zero-phonon and vibronic origins are shown in Figure 5, and the relative intensities and the  $\Delta A/A$  values are given in Table I. A discussion of these quantities and the relevant selection rules is deferred to a later section.

A very weak line with a bandwidth of  $\sim 4 \text{ cm}^{-1}$  was found on the high-energy tail of the middle band. The spectroscopic data for this line are given in Table I and Figure 6. Except for this new feature, the observed spectra are essentially the same as those reported previously<sup>9–13</sup> and a full description can be obtained from these works. An attempt to obtain fluorescence, which has been observed<sup>27</sup> in the dilute crystal  $\text{K}_2\text{Zn}[\text{Cu}]\text{F}_4$ , was unsuccessful.

## Theory and Discussion

**Ligand Field Calculations.** Within a simple orbital-only model, the transition energies of  $\text{CuF}_6^{4-}$  in an tetragonally elongated ligand field are given by

$$\begin{aligned} {}^2B_{1g}(x^2-y^2) &\rightarrow {}^2A_{1g}(z^2) & 2(\sigma_{\perp} - \sigma_{\parallel}) \\ &\rightarrow {}^2B_{2g}(xy) & 3\sigma_{\perp} - 4\pi_{\perp} \\ &\rightarrow {}^2E_g(xz,yz) & 3\sigma_{\perp} - 2(\pi_{\perp} + \pi_{\parallel}) \end{aligned} \quad (2)$$

The symbols  $\sigma$  and  $\pi$  represent the angular overlap model (AOM) parameters  $e_{\sigma}$  and  $e_{\pi}$  and the subscripts  $\parallel$  and  $\perp$  refer to the axial and equatorial bonds, respectively. Related quantities are the "cubic" splitting,  $\Delta$ , between the barycenters of the  $e_g$  and  $t_{2g}$  orbitals and the tetragonal splitting of the  $e_g$  and  $t_{2g}$  orbitals,  $\Delta_e$  and  $\Delta_t$ , as shown in Figure 7. These are given respectively as

$$\begin{aligned} \Delta &= 2\sigma_{\perp} + \sigma_{\parallel} - \frac{4}{3}(2\pi_{\perp} + \pi_{\parallel}) \\ \Delta_e &= 2(\sigma_{\perp} - \sigma_{\parallel}) \\ \Delta_t &= 2(\pi_{\perp} - \pi_{\parallel}) \end{aligned} \quad (3)$$

Since there are four AOM parameters and three observed tran-

sition energies, we set the  $\pi$  bonding proportional to the  $\sigma$  bonding such that  $\pi_{\parallel}/\sigma_{\parallel} = \pi_{\perp}/\sigma_{\perp}$ . The  ${}^2B_{1g}(x^2-y^2) \rightarrow {}^2A_{1g}(z^2)$  transition has been assigned<sup>10–13</sup> to an absorption peak at  $970 \text{ cm}^{-1}$ , which implies only a small  $\sigma$ - but a large  $\pi$ -bonding anisotropy. Equation 2 then gives the physically unrealistic AOM parameters listed in the caption to Figure 7. Also shown are the AOM parameters obtained from the assignment favored in this work.

Apart from this deficiency, the assignment of Kleemann et al. also has difficulty in explaining (a) the magnitude of the intensity of the MCD of the magnetic dipole origin at  $8764 \text{ cm}^{-1}$ , (b) the apparent large separation, about  $2800 \text{ cm}^{-1}$ , of the Franck–Condon maxima for the  ${}^2B_{1g}(x^2-y^2) \rightarrow {}^2B_{2g}(xz)$ ,  ${}^2B_{3g}(yz)$  transitions,<sup>24</sup> which implies a very different displacement of the two potential surfaces along totally symmetric coordinates, and (c) the appearance of a second magnetic dipole origin that gives a splitting of  $1447 \text{ cm}^{-1}$  for their assignment of the  ${}^2B_{2g}(xz)$ ,  ${}^2B_{3g}(yz)$  origins, which is too large to be explained by the combined actions of spin-orbit coupling and an orthorhombic distortion.

The expression for the transition energies given in (2) are only approximate, as they do not include the effects of spin-orbit coupling. Before performing such calculations, it is necessary to estimate the effective spin-orbit coupling constant  $\lambda$ , as this will be reduced from the free-ion value of  $\lambda_0 = 830 \text{ cm}^{-1}$  by covalency effects. This can be done by examining the experimental  $g$  values of the ground state, which differ from the spin-only value because of small admixing of the excited states by spin-orbit coupling.

**Electron Spin Resonance.** The published  $g$  values of  $\text{K}_2\text{CuF}_4$  have been obtained both from ESR<sup>7</sup> and magnetic susceptibility<sup>16</sup> measurements. The  $g$  values below the Curie temperature ( $6.25 \text{ K}$ ) are greatly perturbed by the molecular fields caused by the ferromagnetic ordering of the spins.<sup>7</sup> However, the observed values at  $77 \text{ K}$  do not suffer the effects of long-range order and are  $g_a = 2.279$  and  $g_c = 2.087$ . The absence of any angular dependence of  $g_a$  shows that the  $g$  tensors of the separate sites within the (001) planes are exchange-narrowed.<sup>7</sup> If it is assumed that the site symmetry at the  $\text{Cu}^{2+}$  ion is approximately  $D_{4h}$ , then the crystal and the molecular  $g$  values are related by

$$g_a = \frac{1}{2}(g_{\parallel} + g_{\perp}) \quad g_c = g_{\perp} \quad (4)$$

If we use an electronic basis diagonal in the tetragonal field, then, for a tetragonally elongated  $\text{CuF}_6^{4-}$  complex, the perturbation expressions for the  $g$  values up to third order are

$$\begin{aligned} g_{\parallel}({}^2B_{1g}) &= g_s + 8k'_{\parallel}\lambda'_{\parallel}/E_{xy} - (g_s + k_{\parallel})\lambda'_{\perp}{}^2/E_{xz}{}^2 - 4k'_{\parallel}\lambda_{\perp}\lambda'_{\perp}/E_{xz}E_{xy} \\ g_{\perp}({}^2B_{1g}) &= g_s + 2k'_{\perp}\lambda'_{\perp}/E_{xz} - 2g_s\lambda'_{\parallel}{}^2/E_{xy}{}^2 - \\ &g_s\lambda'_{\perp}{}^2/(2E_{xz}{}^2) + k'_{\perp}\lambda'_{\perp}\lambda_{\parallel}/E_{xz}{}^2 + \lambda'_{\parallel}(k'_{\perp}\lambda_{\perp} - \\ &k_{\perp}\lambda'_{\perp})/E_{xz}E_{xy} \end{aligned} \quad (5)$$

where  $g_s = 2.0023$ ,  $k' = +i\langle t_2\parallel||e\rangle/2\sqrt{3}$ ,  $k = -i\langle t_2\parallel||t_2\rangle/\sqrt{6}$ ,  $\lambda' = +i\langle t_2\parallel v(1T_1)\parallel e\rangle/3\sqrt{2}$ ,  $\lambda = -i\langle t_2\parallel v(1T_1)\parallel t_2\rangle/3$ ,  $E_{xy} = E({}^2B_{2g}) - E({}^2B_{1g})$ , and  $E_{xz} = E({}^2E_g) - E({}^2B_{1g})$ . The reduced matrix elements of the orbital reduction parameter  $k$  and spin-orbit coupling are taken from Sugano et al.<sup>28</sup> Equation 5 takes into account both the cubic anisotropy  $k \neq k'$  and  $\lambda \neq \lambda'$  and the tetragonal anisotropy  $k_{\parallel} \neq k_{\perp}$ ,  $\lambda_{\parallel} \neq \lambda_{\perp}$ , and  $E_{xy} \neq E_{xz}$ .

It is customary to ignore the cubic anisotropy in the  $k$  and  $\lambda$  parameters. If we assume that  $\lambda_{\alpha} \approx k_{\alpha}\lambda_0$ , where  $\lambda_0$  ( $\sim 830 \text{ cm}^{-1}$ ) is the spin-orbit coupling constant for the  $\text{Cu}^{2+}$  free ion, then (5) reduces to

$$\begin{aligned} g_{\parallel}({}^2B_{1g}) &= g_s + 8k_{\parallel}v_{\parallel} - (g_s + k_{\parallel})v_{\perp}{}^2 - 4k_{\perp}v_{\parallel}v_{\perp} \\ g_{\perp}({}^2B_{1g}) &= g_s + 2k_{\perp}v_{\perp} - 2g_s v_{\parallel}{}^2 - \frac{1}{2}g_s v_{\perp}{}^2 + k_{\parallel}v_{\perp}{}^2 \\ v_{\parallel} &= k_{\parallel}\lambda_0/E_{xy} \quad v_{\perp} = k_{\perp}\lambda_0/E_{xz,yz} \end{aligned} \quad (6)$$

Similar expressions given by other authors<sup>7,29,30</sup> have errors in the

(26) Riley, M. J.; Hitchman, M. A. *Inorg. Chem.* **1987**, *26*, 3205.

(27) Dubicki, L.; Krausz, E. R.; Riley, M. J.; Yamada, I. *Chem. Phys. Lett.* **1989**, *157*, 315.

(28) Sugano, S.; Tanabe, Y.; Kamimura, H. *Multiplets of Transition Metal Ions in Crystals*; Academic Press: New York, 1970.

(29) Riley, M. J.; Hitchman, M. A.; Reinen, D. *Chem. Phys.* **1986**, *102*, 11.

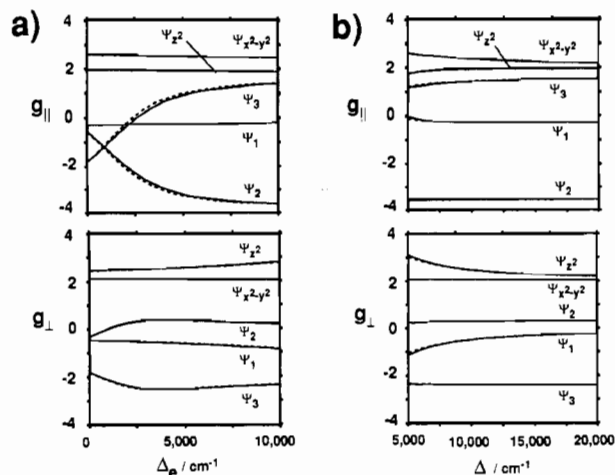


**Figure 8.** Calculated  $g$  values for  ${}^2E$  and  ${}^2T_2$  multiplets from numerical diagonalization (full lines) and the perturbation formula given in Table VI (dashed lines) (a) as a function of the tetragonal ligand field and constant cubic field,  $\Delta = 7000 \text{ cm}^{-1}$ , and (b) as a function of the "cubic" ligand field and a constant tetragonal field,  $\Delta_e = 8400 \text{ cm}^{-1}$ . The wave functions  $\Psi_1$ ,  $\Psi_2$ , and  $\Psi_3$  for the  ${}^2T_2$  multiplet are defined in Table V. Note that the  $g$  values at a given value of  $\Delta$  and  $\Delta_e$  refer to a nuclear geometry that is identical for both  ${}^2E$  and  ${}^2T_2$  states.

third-order terms; however, it is noted that, for cases where  $k$  is close to 1, the quantitative difference between eq 6 and the expressions given in refs 7, 29, and 30 is small. Equations 5 and 6 have been derived on the basis that the nuclear geometry of the ground and the  ${}^2T_2$  states are identical, so that the energy separations  $E_{xy}$  and  $E_{xz}$  should be obtained from the Franck-Condon maxima of the absorption spectra.

If we use the spectroscopic data in Table I and ignore tetragonal anisotropy in  $k$ , then (6) gives a reasonable fit to the experimental  $g$  values; viz.,  $g_{||} = 2.49$  and  $g_{\perp} = 2.08$  for  $k = 0.85$  compared with  $g_{|| \text{ obs}} = 2.47$  and  $g_{\perp \text{ obs}} = 2.09$ . This agreement provides strong evidence that the site symmetry at the copper ion is close to  $D_{4h}$  and that the orthorhombic distortion is indeed very small. The value  $k = 0.85$  implies only a small degree of covalency in the ground state, as expected for an ionic ligand such as  $F^-$  and is in agreement with values obtained from other  $CuF_4^{2-}$  studies.<sup>29,31</sup>

It is instructive to extend the above analysis to  $KCuF_3$ . Just as for  $K_2CuF_4$ , the structure of  $KCuF_3$  consists of planes of "antiferrodistortive"  $CuF_6$  octahedra. However, in  $KCuF_3$ , the terminal fluoride ions bridge the  $Cu^{2+}$  ions and form antiferromagnetically coupled linear chains,  $\dots F-Cu-F-Cu-F \dots$ , along the crystal  $c$  axis. An ordered stacking<sup>32</sup> of the  $c$  planes give crystals called type d, which have the crystal  $g$  values  $g_a = 2.25$  and  $g_c = 2.16$ . An alternate stacking<sup>32</sup> gives crystals of type a, which have  $g_a = 2.28$  and  $g_c = 2.16$ . The average  $g$  values,  $\bar{g} = (g_c + 2g_a)/3$ , are 2.22 and 2.24 for type d and a crystals, respectively. These values compare favorably with  $\bar{g} = 2.22$  for  $K_2CuF_4$ . On the other hand, the crystal  $g$  values of  $KCuF_3$  cannot be explained by using (4) and (6). This implies that the orthorhombic distortion in  $KCuF_3$  is very large, a result that is consistent with the X-ray structural data,<sup>33</sup> the Cu-F bond lengths being 189, 196, and 225 pm.

**Simulation of the Magneto-Optical Spectra of the Zero-Phonon Transitions.** We have calculated the magneto-optical spectra of the zero-phonon lines by diagonalizing the full  $10 \times 10$  energy matrix as described in Appendix A1. The simulated spectra are given in Figures 8-13 and agree very closely with a simple perturbation model that ignores the mixing of the electronic states by the magnetic fields. The overall optical absorption spectrum of  $K_2CuF_4$  does not change when the crystal becomes ferromagnetic, as the exchange interactions between copper ions are

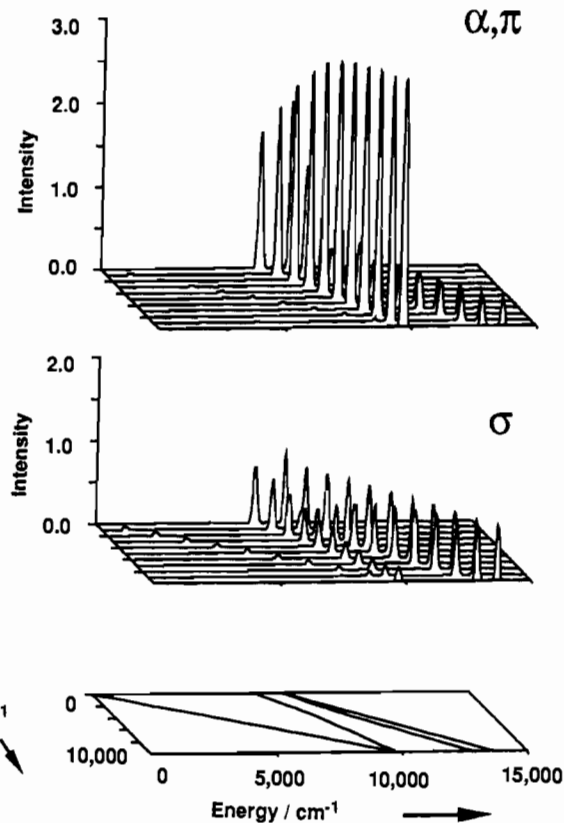


**Figure 9.** Calculated magnetic dipole strengths in  $\alpha$ ,  $\pi$ , and  $\sigma$  polarizations as a function of the tetragonal ligand field,  $\Delta_e$ . The "cubic" field is held constant ( $\Delta = 7000 \text{ cm}^{-1}$ ). The internal exchange field,  $B_{ex}$ , is parallel to  $a$  although on this energy scale the calculation is indistinguishable from the case of zero internal field. The magnetic dipole strengths follow from (1) and (7), where  $k = 0.85$  and are in units of Bohr magnetons squared.

small compared to the ligand field, but the sharp line fine structure is greatly influenced by the internal magnetic field.

Diagonalization of the zero field energy matrix gives the eigenstates, in order of increasing energy,  $\Psi_{x^2-y^2}(\Gamma_7)$ ,  $\Psi_{z^2}(\Gamma_6)$ ,  $\Psi_3(\Gamma_7)$ ,  $\Psi_2(\Gamma_7)$ , and  $\Psi_1(\Gamma_6)$ . For large  $\Delta_e$ , as is the case of  $K_2CuF_4$ ,  $\Psi_1$  and  $\Psi_2$  approximate the Russell-Saunders wave function  ${}^2E_g$ , while  $\Psi_3$  becomes  ${}^2B_{2g}$ . Each Kramer's doublet transforms under rotations as  $|J = 1/2, M_J = \pm 1/2\rangle$ . Their explicit form is given in Table V.

The sign of the  $g_{||}$  values (Figure 8) is fixed by symmetry.<sup>34</sup> The sign of  $g_{\perp}$  is arbitrary and depends on the phases of the wave functions. We have used the coupling coefficients of Koster et al.<sup>35</sup> in constructing the spin-orbit basis (A.1.1). This choice gives the sign of  $g_{\perp}$  as shown in Figure 8 and the magnetic dipole selection rules  $\Delta M_J = 0$  for  $H \parallel B$  and  $\Delta M_J = \pm 1$  for  $H \perp B$ , where  $\alpha$  is the direction of spin quantization, parallel to  $B$ , and  $H$  is the magnetic field vector of the incident light. The sign of the  $g$  values, the  $\Delta M_J$  selection rules, and Table VII provide a simple explanation of the Zeeman splittings described in later sections.

The observed polarization,  $\alpha = \pi \neq \sigma$ , identifies the sharp lines at 8764 and 10214  $\text{cm}^{-1}$  as magnetic dipole origins (Table I). The dipole strengths were obtained from (1) and (7), where  $\Psi_g$  and

$$M_{\alpha} = |\langle \Psi_g | m_{\alpha} | \Psi_e \rangle|^2 = |\langle \Psi_g | k_{\alpha} l_{\alpha} + g_s s_{\alpha} | \Psi_e \rangle|^2 \quad (7)$$

$\Psi_e$  are the ground- and excited-state wave functions, respectively,  $g_s = 2.0023$ , and  $k_{\alpha} = 0.85$ . The calculated absorption spectra with ferromagnetic saturation along the  $a$  axis are shown in Figure 9. They are nearly identical with the calculated zero-field ab-

(30) Friebel, C.; Propach, V.; Reinen, D. *Z. Naturforsch.* **1976**, *31B*, 1574.  
 (31) Kubo, H.; Yahara, I.; Hirakawa, K. *J. Phys. Soc. Jpn.* **1976**, *41*, 442.  
 (32) Ikebe, M.; Date, M. *J. Phys. Soc. Jpn.* **1971**, *30*, 93.  
 (33) Okazaki, A.; Suemune, Y. *J. Phys. Soc. Jpn.* **1961**, *16*, 176.

(34) Pryce, M. H. L. *Phys. Rev. Lett.* **1959**, *3*, 375.  
 (35) Koster, G. F.; Dimmock, J. O.; Wheeler, R. G.; Statz, H. *Properties of the Thirty-Two Point Groups*; MIT Press: Cambridge, MA, 1963.

**Table III.** Magnetic Dipole Selection Rules for Orbital and Spin-Orbit Bases in Local  $D_{4h}$  Symmetry

orbital states				spin-orbit states			
transition	$M_{x,y}^a$	$M_z$	$\alpha, \pi^b$	transition	$M_{x,y}$	$M_z$	$\alpha, \pi$
${}^2B_{1g}(x^2 - y^2) \rightarrow$			$\sigma$	$\Gamma_7(x^2 - y^2) \rightarrow$			
${}^2A_{1g}(z^2)$				$\Gamma_6(z^2)$	✓		✓ ✓
${}^2B_{2g}(xy)$	✓	✓		$\Gamma_7(xy)$	✓	✓	✓ ✓
${}^2E_g(xz, yz)$	✓		✓ ✓	$\Gamma_7(xz, yz)$	✓	✓	✓ ✓
				$\Gamma_6(xz, yz)$	✓		✓ ✓

<sup>a</sup>  $M_{x,y}$  and  $M_z$  are the magnetic dipole strengths with the magnetic vector of incident light parallel to the molecular  $x$ ,  $y$ , and  $z$  axes, respectively.  
<sup>b</sup> The crystal polarizations are defined in (1).

sorption spectra and are consistent with the magnetic dipole selection rules given in Table III.

Figure 9 shows that while all transitions are allowed in  $\alpha$ ,  $\pi$ , and  $\sigma$  polarizations, in agreement with the spin-orbit selection rules, the intensities follow closely the orbital selection rules. In particular, for large values of  $\Delta_e$  the calculated ratio of the intensities for the  $\Psi_{x^2-y^2} \rightarrow \Psi_3$  and  $\Psi_{x^2-y^2} \rightarrow \Psi_1, \Psi_2$  transitions approaches a value of 4 in  $\alpha$  polarization, as expected for the Russell-Saunders limit. A more detailed spectroscopic study of the origins is given in the next three sections.

**Magnetic Circular Dichroism.** The direction of the incident light and the applied magnetic field are parallel to the crystal  $c$  axis for the measurement of MCD. In this case, the ferromagnetic saturation is transverse to the approximate  $D_{4h}$  local symmetry of the  $\text{Cu}^{2+}$  ions. According to Table III, nonvanishing transverse MCD will occur only for two zero-phonon transitions,  $\Psi_{x^2-y^2}(\Gamma_7) \rightarrow \Psi_3(\Gamma_7)$  and  $\Psi_{x^2-y^2}(\Gamma_7) \rightarrow \Psi_2(\Gamma_7)$ , and originate from the "interference" between  $m_z$  and  $m_x$  transition magnetic dipoles.

The differential circularly polarized magnetic dipole strength and the total magnetic dipole strength are given by

$$\Delta M = |\langle \Psi_g | m_- | \Psi_e \rangle|^2 - |\langle \Psi_g | m_+ | \Psi_e \rangle|^2$$

$$M = |\langle \Psi_g | m_- | \Psi_e \rangle|^2 + |\langle \Psi_g | m_+ | \Psi_e \rangle|^2 \quad (8)$$

where  $m_{\pm} = \mp(1/2)^{1/2}(m_z \pm im_x)$ . Both copper sites have an identical MCD spectrum, since they are related by a  $C_4$  axis parallel to the  $c$  axis, and only one of the sites need be considered in the calculations. The quantities  $\Delta M$  and  $M$ , in units of Bohr magnetons squared, are plotted as a function of  $\Delta_e$  in Figure 10.

Figures 9 and 10 show that the observed magnetic dipole origins must be assigned to the  $\Psi_{x^2-y^2}(\Gamma_7) \rightarrow \Psi_3(\Gamma_7)$ ,  $\Psi_2(\Gamma_7)$  transitions, in agreement with the assignment made from simple structure-bonding arguments. There is no alternative assignment for the strong negative MCD signal at 8764  $\text{cm}^{-1}$  and the weak positive signal at 10214  $\text{cm}^{-1}$ .

The observed intensity ratio of the weak and strong magnetic dipole origins is  $\sim 0.016$ , which disagrees with the calculated relative intensities in Figures 9 and 10. This is not unexpected, since the calculations have been made for pure electronic rather than vibronic states. Large geometry changes in the excited states are expected as an electron is promoted into the  $x^2 - y^2$  orbital, which points directly at the equatorial ligands. Such a geometry change will reduce the intensity of an origin by a vibrational overlap, or reduction factor. The effects of these geometry changes are considered after we examine the vibrational fine structure of the  $\Psi_{x^2-y^2} \rightarrow \Psi_3$  transition.

It should be noted that the  $\Delta M/M$  values will not be reduced, as the same vibrational factors enter into both the numerator and denominator of the ratio. These then represent important experimental quantities, and the observed values in Table I are in excellent agreement with those calculated confirming the present assignment. For the parameters  $\Delta = 7000 \text{ cm}^{-1}$  and  $\Delta_e = 8000 \text{ cm}^{-1}$ , the calculated values of  $\Delta M/M$  are  $-0.30$  and  $+0.74$  for the  $\Psi_{x^2-y^2} \rightarrow \Psi_3$  and  $\Psi_{x^2-y^2} \rightarrow \Psi_2$  transitions, respectively.

**Zeeman and MLD Spectra of the 8764- $\text{cm}^{-1}$  Origin.** The effect of an applied magnetic field in the (001) plane on the origin at 8764  $\text{cm}^{-1}$  has been studied in detail<sup>12,13</sup> and is consistent with our assignments. Following the work of Ferré et al.,<sup>13</sup> an angle

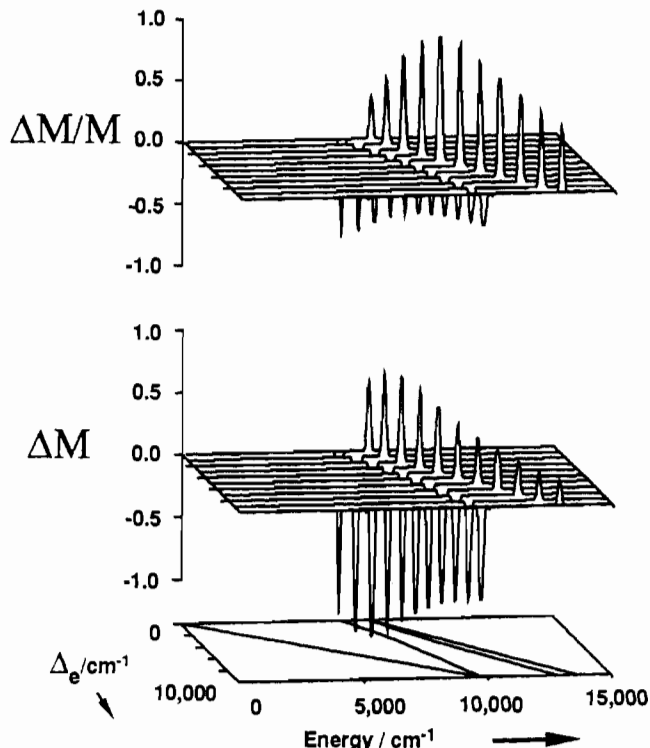


**Figure 10.** Calculated MCD spectrum as a function of the tetragonal ligand field,  $\Delta_e$ . The "cubic" field is held constant ( $\Delta = 7000 \text{ cm}^{-1}$ ).  $\Delta M$  refers to the differential magnetic dipole strengths given in (8). Note that two transitions are forbidden in transverse MCD.

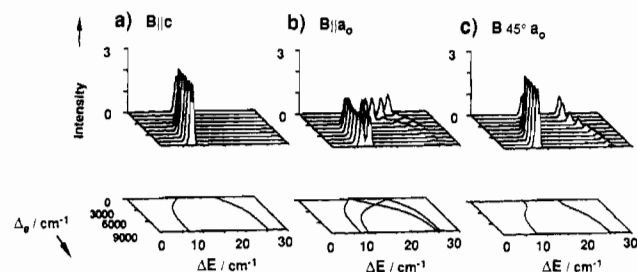


**Figure 11.** Zeeman splittings of the 8764- $\text{cm}^{-1}$  origin in an external field of 5 T: (a)  $\alpha$  polarization ( $B \parallel c$ ); (b)  $\alpha$  polarization ( $B \parallel a_0$ ;  $\beta = 0^\circ$ ); (c)  $\alpha$  polarization ( $B$  at  $45^\circ$  to  $a_0$ ;  $\beta = 45^\circ$ ). The internal magnetic field,  $B_{\text{ex}}$ , is 30 T in the  ${}^2E_g$  multiplet and 15 T in the  ${}^2T_{2g}$  multiplet (see text). The spectra are calculated by assuming only the lowest Zeeman components of the ground state is populated, corresponding to the low-temperature limit.  $\Delta E$  is the energy difference of the spectra calculated with the applied and internal magnetic fields and the (hypothetical) spectra calculated in the absence of any magnetic fields. The average position of the transitions shifts to higher energy because of the ground-state Zeeman energy.

$\beta$  is defined as that which the magnetic field direction makes with the  $a_0$  axes in the (001) plane. The two important directions are  $\beta = 0^\circ$  ( $B \parallel a_0$ ) and  $\beta = 45^\circ$ . For  $\beta \neq 45^\circ$  each electronic state will split into four components because of the inequivalent  $g$  values of the two copper sites. Unlike the EPR spectrum, which is exchange-narrowed,<sup>7</sup> the electronic transitions occur on a faster time scale and give the superimposed Zeeman spectrum of each site.

Figure 11 shows the Zeeman splitting of the 8764- $\text{cm}^{-1}$  origin calculated as a function of  $\Delta_e$  for (a)  $B \parallel c$ , (b)  $B \parallel a_0$  ( $\beta = 0^\circ$ ), and (c)  $B$  at  $45^\circ$  to  $a_0$  ( $\beta = 45^\circ$ ). In the axial field case (Figure 11a) the spin is quantized along the  $c$  axis. The Zeeman levels of both sites are separated by approximately  $g_{\perp} \mu_B B$ , where the  $g_{\perp}$  values are given in Table VI and Figure 8. For both  $B \parallel c$  and  $\beta = 45^\circ$  the equal Zeeman splitting of the two copper centers in the unit cell is independent of the local symmetry (Figure 2). The distribution of intensity in Figure 11a is easily understood by noting that  $g_{\perp}(\Psi_3)$  is negative and  $\Delta M_f^c = \pm 1$ , since  $H \perp B$  for a polarization with  $B \parallel c$ .

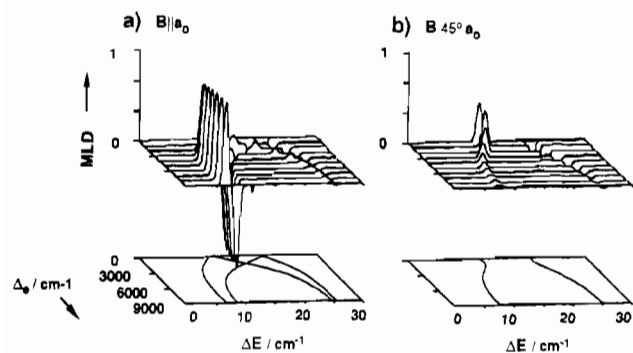


**Figure 12.** Magnetic linear dichroism of the 8764-cm<sup>-1</sup> origin in an external field of 5 T in the (001) plane: (a)  $\alpha$  polarization ( $B \parallel a_0$ ;  $\beta = 0^\circ$ ); (b)  $\alpha$  polarization ( $B$  at  $45^\circ$  to  $a_0$ ;  $\beta = 45^\circ$ ). Other quantities are defined as in Figure 11.

A very small energy shift is expected for the  $\Psi_{x^2-y^2} \rightarrow \Psi_3$  origin in the absence and presence of an applied magnetic field  $B \parallel c$ . This corresponds to the difference in the line energies given in Figure 11a,c. Experimentally, a shift of only 1 cm<sup>-1</sup> was observed.<sup>13</sup> The bandwidth of the origin at 8764 cm<sup>-1</sup> was also observed to decrease from 5.5 to 3.9 cm<sup>-1</sup> as  $\beta$  was varied from 0 to 45°.<sup>13</sup> This observation is simply explained by the calculated spectra shown in Figure 11b,c. For  $\beta = 45^\circ$  the intensity is located predominantly in a single peak that should have an intrinsic line width of 3.9 cm<sup>-1</sup>, while for  $\beta = 0^\circ$  there are two close-lying peaks of equal intensity. Furthermore, the small peak observed<sup>13</sup> at  $\sim 8$  cm<sup>-1</sup> to higher energy is qualitatively reproduced in the calculated spectra (Figure 11b,c) in both position and relative intensity.

The MLD is the difference in absorption for the electric vector of light polarized parallel and perpendicular to the direction of the magnetic field where the direction of the light propagation is always at right angles to the magnetic field. The calculated MLD is shown in Figure 12. The calculations agree with experiment,<sup>13</sup> where, for  $\beta = 0^\circ$ , a large positive peak is followed by a negative one at higher energy and the MLD disappears when the magnetic field is rotated to  $\beta = 45^\circ$ .

The splitting of the lines that cause the broadening of the strong origin shown in Figure 11b is of the order 2.5 cm<sup>-1</sup>. However, there are several reasons why this is an unreliable quantity to use in quantifying the size of the internal field of the  $\Psi_3$  excited state. First, it can be seen from Figure 11b that this splitting is dependent on the tetragonal ligand field, a quantity that is not known for this electronic state other than being considerably less than the  $\Delta_c \sim 8000$  cm<sup>-1</sup> estimated for the ground equilibrium geometry. Second, the calculated splitting of the lines is relatively independent of the magnetic field strength as each line arises from one component of the Zeeman splitting of each site. This means that while the Zeeman splitting of each site increases with the field, the energy difference between the two lower components of these splittings is insensitive to the field.

By using the splitting between the main origin and the weak satellite 8 cm<sup>-1</sup> to higher energy to quantify the internal field, one can avoid many of the complications given above. This splitting is approximately independent of the size of the field in the ground state, a result that is exact for  $\beta = 45^\circ$  as the  $g$  values are equal for both sites in this direction. The splitting is relatively insensitive to the size of the tetragonal field and together with the Zeeman experiments on the 10214-cm<sup>-1</sup> origin, gives a value of  $15 \pm 5$  T for the internal field.

**Zeeman Spectra of the 10214-cm<sup>-1</sup> Origin.** The calculated transverse Zeeman spectra (light perpendicular to  $c$ ) of the 10214-cm<sup>-1</sup> origin are given in Figure 13. The spectra shown in Figure 13a mimic the observed behavior of the magnetic dipole origin in the absence of an applied field shown in Figure 6. In  $\pi$  polarization the origin is split into two peaks separated by  $\sim 10$  cm<sup>-1</sup>, while in  $\sigma$  polarization a single more intense peak is observed nearly coincident with the peak at lower energy in the  $\pi$  spectrum. When the field is directed parallel to the  $c$  axis, the  $\pi$  spectrum collapses into a single peak midway between the two peaks that

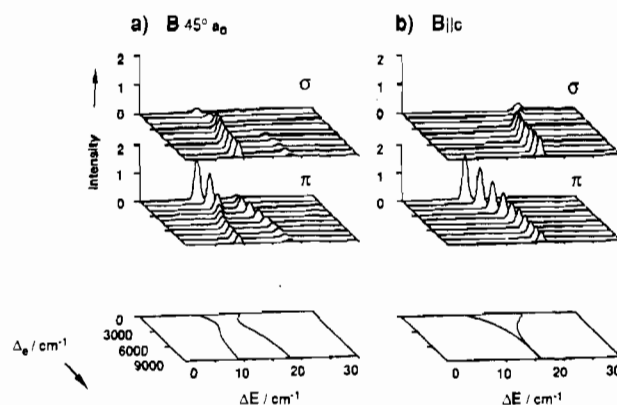


**Figure 13.** Transverse absorption and Zeeman spectra of the 10214-cm<sup>-1</sup> origin in (a) zero-applied field and (b) an external field of 5 T applied along the  $c$  axis. The internal exchange field for the  ${}^2E_g$  and  ${}^2T_{2g}$  multiplets were taken as 30 and 15 T, respectively.

were calculated for  $\beta = 45^\circ$ . In the case of the  $\sigma$  spectrum, a single peak is calculated for  $B \parallel c$  that is shifted  $\sim 7$  cm<sup>-1</sup> to higher energy compared to the spectra calculated for  $\beta = 45^\circ$ . These predictions agree precisely with the experimental data in Figure 6.

The  $\pi$  spectrum is then an unusual case where there is an observed Zeeman splitting in the absence of an applied magnetic field that apparently disappears when a magnetic field is applied parallel to  $c$ . This distribution of intensity is simply explained by noting that  $g_\perp(\Psi_2)$  is positive and for  $\pi$  polarization  $H \perp B$  and  $\Delta M_j^z = \pm 1$ , while for  $\sigma$  polarization  $H \parallel B$  and  $\Delta M_j^z = 0$ . The magnitude of the Zeeman splitting in Figure 13b is quenched by the tetragonal field, and the observed separation of the peak in  $\sigma$  and  $\pi$  polarizations with  $B \parallel c$  is  $\sim 4$  cm<sup>-1</sup> from Figure 6. The experimental splittings can best be reproduced with a magnetic field of  $B \sim 15 \pm 5$  T and a tetragonal ligand field of  $\Delta_c \sim 3000 \pm 1000$  cm<sup>-1</sup>.

**Vibrational Fine Structure.** The extensive vibrational fine structure of the  $\Psi_{x^2-y^2}(B_{1g}) \rightarrow \Psi_3(B_{2g})$  transition is shown in Figure 4 and analyzed in Table II. The vibronic origin with an energy of 213 cm<sup>-1</sup> is of particular importance. As noted by Kleemann and Farge,<sup>11</sup> it is electric dipole allowed,  $\alpha \approx \sigma \neq \pi$ , and accordingly it must be an ungerade vibration.

The  $\pi$  intensity of this vibronic origin is close to zero, which implies that it is  $z$  polarized in the  $D_{4h}$  site group, and with use of orbital selection rules, the vibration should be of  $B_{1g} \otimes A_{2u} \otimes B_{2g} = A_{1u}$  symmetry. However, a vibration transforming as this irreducible representation *does not exist* for a  $D_{4h}$   $CuF_6^{4-}$  complex. This is thought to be the principal reason why Kleemann et al.<sup>10-13</sup> have made the assignment given in Figure 7b. They utilized the  $D_{2h}$  site group and assigned the 8764-cm<sup>-1</sup> origin as the  ${}^2A_{1g}(x^2 - y^2) \rightarrow {}^2B_{3g}(yz)$  transition and the 213-cm<sup>-1</sup> phonon as having  $b_{2u}$  symmetry.<sup>36</sup> This assignment means, in terms of the local  $D_{4h}$  symmetry, that the magnetic dipole origin corresponds to one component of the  ${}^2E_g$  state and the vibronic origin corresponds to one component of an  $e_u$  vibration.

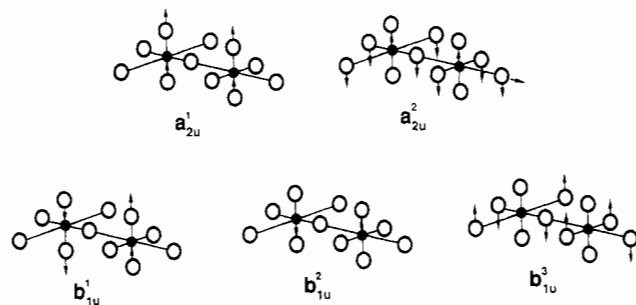
The vibronic origin then appears to be a strong argument against the assignment proposed in the present work. The dilemma is not resolved by considering the vibronic selection rules in the spin-orbit  $D_{4h}$  double group. In this case there is no vibration that gives  $\alpha$ - and  $\sigma$ -polarized intensity without allowing  $\pi$ -polarized intensity as well. Since experimentally  $\alpha = \sigma \gg \pi$ , it is clear that the vibration is mainly  $z$  allowed in the molecular coordinate system with the small amount of observed  $xy$  character being due to the spin-orbit mixing of the electronic states. The calculations of the previous section have shown that the effects of spin-orbit mixing are secondary in importance and to a good approximation

(36) Cotton, F. A. *Chemical Applications of Group Theory*; Wiley: New York, 1971. References 11 and 13 use a nonconventional  $D_{2h}$  point group. Here a  $D_{2h}$  point group is used where  $xy, xz, yz$  transform as  $B_{1g}, B_{2g},$  and  $B_{3g}$ , respectively.

**Table IV.** Vibronic Selection Rules for Single-Ion and Factor Group Orbital Bases in  $K_2CuF_4$ 

	single-ion orbital states <sup>a</sup>		factor group states <sup>b</sup>		
	$\alpha, \sigma$	$\pi$	$\alpha, \sigma$	$\pi$	
${}^2B_{1g} \rightarrow$			${}^2A_{1g} \rightarrow$		
${}^2A_{1g}$	$b_{2u}, e_u$	$e_u$	$e_u$	$a_{2u}$	$b_{1u}$
${}^2B_{2g}$	$e_u$	$e_u$	$e_u$	$e_u$	$e_u$
${}^2E_g$	$a_{2u}, b_{2u}$	$a_{2u}, b_{2u}$	$a_{2u}, b_{1u}$	$a_{2u}, b_{1u}$	$e_u$
	$e_u$		$e_u$	$e_u$	$e_u$
			$e_u$	$a_{2u}, b_{1u}$	$e_u$
			$e_u$	$a_{2u}, b_{1u}$	$e_u$

<sup>a</sup>The odd parity molecular vibrations are  $2a_{2u}, b_{2u}$ , and  $3e_u$  for a  $CuF_6^{4-}$  chromophore with  $D_{4h}$  local symmetry. The  $z$  axis is perpendicular to the crystal  $c$  axis (Figure 2). The crystal polarizations  $\alpha, \sigma$ , and  $\pi$  are defined in (1). <sup>b</sup>The odd parity lattice vibrations are  $3a_{2u}, 4b_{1u}$ , and  $7e_u$  for the  $D_{4h}$  unit cell of  $K_2CuF_4$  (Table VIII and Figure 18).

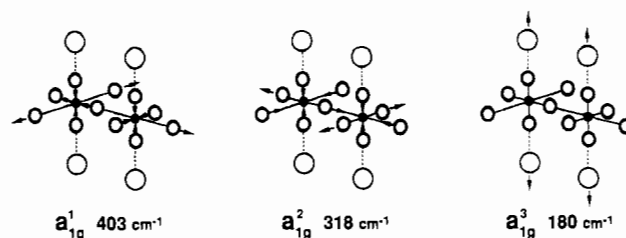
**Figure 14.** Symmetry coordinates that form a basis for the lattice modes of  $a_{2u}$  and  $b_{1u}$  symmetry, neglecting those that only involve movement of the  $K^+$  ions.

the electronic states retain their orbital characteristics. The corresponding vibronic selection rules are given in Table IV.

In the Raman studies of Natsume and Yamada,<sup>15</sup> it was necessary to interpret the ground vibrational spectrum in terms of the lattice modes of the crystal rather than the molecular vibrations of the  $CuF_6^{4-}$  units. A factor group analysis (Appendix A2) gives the symmetries of the electronic and vibrational states in terms of their irreducible representations of the  $D_{4h}$  factor group of the crystal. There are ungerade modes of  $a_{2u}, b_{1u}$ , and  $e_u$  symmetry, and the vibronic selection rules are given in Table IV. It can be seen that the  $\alpha$ - and  $\sigma$ -polarized vibronic origin at  $8977\text{ cm}^{-1}$  is due to an ungerade mode of either  $a_{2u}$  or  $b_{1u}$  symmetry.

From (A2.1) there are seven factor group vibrations that have the appropriate symmetry, and it may seem difficult to unambiguously identify the form of the active mode. However, we assume that the modes involving predominantly the motion of the  $K^+$  ions will be unimportant in the present case, and the symmetry coordinates that form a basis for the remaining five vibrations are shown in Figure 14.

The  $a_{2u}$  vibrations are in-phase and can be compared to the lattice vibrations of crystals with the  $K_2NiF_4$  structure, where the studies of  $K_2MnF_4$  represent the most complete assignment available.<sup>37</sup> The energies of the  $a_{2u}^1$  and  $a_{2u}^2$  vibrations of  $K_2MnF_4$  occur at  $329$  and  $230\text{ cm}^{-1}$ , respectively. The in-phase  $b_{1u}^2$  mode corresponds to the single  $b_{2u}$  mode of  $K_2MnF_4$ , which is calculated to occur at  $95\text{ cm}^{-1}$ , while the out-of-phase  $b_{1u}^1$  and  $b_{1u}^3$  modes correspond to the  $a_{2u}$   $K_2MnF_4$  mode ( $k \neq 0$ ) mode of  $329\text{ cm}^{-1}$ . On energetic grounds it appears that the  $a_{2u}^2$  symmetry coordinate in Figure 14 ( $\approx 230\text{ cm}^{-1}$  in  $K_2MnF_4$ ) should be the most appropriate assignment for the  $213\text{-cm}^{-1}$  vibronic origin in  $K_2CuF_4$ . This conclusion agrees with vibronic studies<sup>38</sup> of square-planar  $CuCl_4^{2-}$ , where it is the bending rather than the stretching ungerade vibration of the same symmetry that provides vibronic electric dipole intensity for the  $\Psi_{x^2-y^2} \rightarrow \Psi_3$  transition.

**Figure 15.** Three symmetry coordinates that form a basis for the  $a_{1g}$  lattice modes of  $K_2CuF_4$ . The vibrational frequencies shown are those observed in the Raman spectrum.<sup>15</sup>

In the Raman spectrum<sup>14,15</sup> of  $K_2CuF_4$ , all three of the  $a_{1g}$  optical modes (Appendix A2) have been identified. They occur at the energies of  $403, 318$ , and  $180\text{ cm}^{-1}$ , and the symmetry coordinates that form a basis for their normal modes are shown in Figure 15. The  $\Psi_{x^2-y^2} \rightarrow \Psi_3$  transition has two  $a_{1g}$  modes based on both the magnetic dipole and vibronic origins, with energies of  $398$  and  $307\text{ cm}^{-1}$  (see Figure 4). They are easily identified as totally symmetric vibrations because their polarization properties and the sign of the MCD reflect those of the origin on which they are built. They can be associated with the ground-state  $a_{1g}$  modes of  $403$  and  $318\text{ cm}^{-1}$ , respectively, as excited-state vibrations are usually reduced from their ground-state values.

The third  $a_{1g}$  mode of  $180\text{ cm}^{-1}$  was not observed in the absorption spectrum. This is in agreement with the work of Natsume and Yamada,<sup>15</sup> who suggested that this mode is composed predominantly of the symmetry coordinate  $a_{1g}^3$  shown in Figure 15. The coupling of the  $a_{1g}^3$  mode with electronic states localized on the  $Cu^{2+}$  ion should be small, since this vibration mainly involves the motion of the  $K^+$  ions.

**Vibronic Reduction Factors.** The vibronic reduction factors represent parameters in an effective Hamiltonian of pure electronic functions, where the vibrational parts of the wave function have not been included. Instead of the electronic transitions occurring as single sharp lines in the  $K_2CuF_4$  spectrum, the intensity of the transitions are spread over a large broad vibrational sideband. These broad bands will consist of multiple excitations of totally symmetric modes and single excitations of odd-parity modes inducing electric dipole intensity as discussed in the previous section. The excitation of the totally symmetric modes is due to a large change in the excited-state geometry, which will then give rise to a progression of nonzero Franck-Condon overlaps. The greater the distortion in the excited state, the smaller will be the intensity of the zero-phonon line.

The ratio of the intensities of the zero-phonon lines of two transitions,  $I_1$  and  $I_2$ , with different displacements,  $D_1$  and  $D_2$ , along a single effective coordinate will be proportional to the factor

$$I_1/I_2 \propto \exp[-\frac{1}{2}(D_1^2 - D_2^2)] \quad (9)$$

where the displacement,  $D$ , has dimensionless units and is related to the Huang-Rhys parameter,<sup>39</sup>  $S$ , through the relation

$$S = \frac{1}{2}D^2 \quad (10)$$

At low temperature the intensity of the  $n$ th member of a progression at an energy of  $E_{0n}$  relative to the origin at  $E_{00}$  is given by<sup>40</sup>

$$I_{0n}/I_{00} \propto (E_{0n}/E_{00})D^{2n}/(2^n n!) \\ D = (1.722 \times 10^{-3})[M(h\nu)]^{1/2}\Delta Q \quad (11)$$

where  $\Delta Q$  is the displacement of the symmetry coordinates in picometers,  $M$  is the inverse of the appropriate  $G$  matrix element<sup>41</sup> in atomic mass units, and  $h\nu$  is the vibrational frequency in reciprocal centimeters. For the two  $a_{1g}$  vibrational modes occurring

(37) Bürger, H.; Strobel, K.; Geick, R.; Müller-Lierheim, W. *J. Phys. C* **1976**, *9*, 4213.

(38) McDonald, R. G.; Hitchman, M. A. *Inorg. Chem.* **1986**, *25*, 3273.

(39) Markham, J. J. *Rev. Mod. Phys.* **1959**, *31*, 956.

(40) McCoy, E. F.; Ross, I. G. *Aust. J. Chem.* **1962**, *15*, 573.

(41) Cyvin, S. J. *Molecular Vibrations and Mean Square Amplitudes*; Elsevier: Amsterdam, 1968.

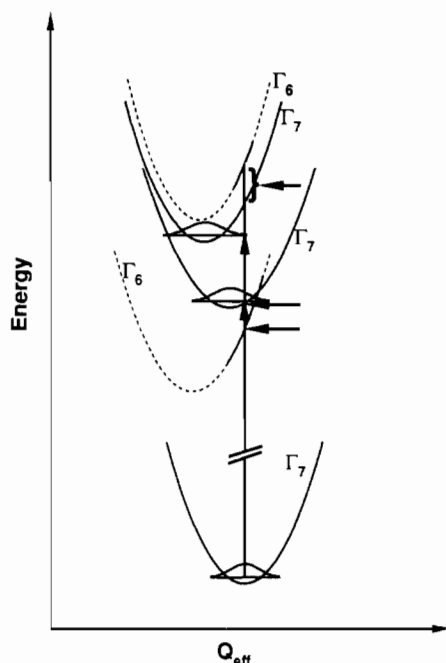


**Figure 16.** Approximate excited-state potential energy surfaces calculated for  $K_2CuF_4$  along an effective  $a_{1g}$  coordinate (see text). The vertical arrows indicate the magnetic dipole origins, while the horizontal arrows indicate the energy of the Franck-Condon maxima.

at 307 and 398  $cm^{-1}$  in the  $\Psi_{x^2-y^2} \rightarrow \Psi_3$  transition, the intensity of the first member relative to the origin is 0.22 and 0.35, respectively. Equation 11 then gives the dimensionless displacements of  $D = 0.66$  and  $0.84$ . Within the semiclassical approximation<sup>39</sup> these numbers give a single effective frequency of  $h\nu \approx 368$   $cm^{-1}$  and an effective displacement of 1.07.

The displacement  $D$  of a single effective mode can also be related to the energy interval between the origin and the band maxima,  $\Delta E$ , as well as the half-width,  $\Delta H$ , for broad bands without structure according to<sup>39</sup>

$$D = \left( 2 \frac{\Delta E}{h\nu} + 1 \right)^{1/2}$$

$$D = \frac{\Delta H}{2h\nu(\ln 2)^{1/2}} \quad (12)$$

Assuming that the broad band centered at 12 140  $cm^{-1}$  is due entirely to the vibrational sideband of the weak origin at 10 214  $cm^{-1}$ , the application of (12) gives the calculated displacements of  $D = 3.4$  and  $D = 4.1$  for the respective equations. The different displacements of  $D \approx 1.1$  and  $D \approx 3.7$  for the  $\Psi_{x^2-y^2} \rightarrow \Psi_3$ ,  $\Psi_2$  transitions, respectively, result in the vibronic reduction of their intensity ratio by the factor 0.0019, according to (9).

The calculated intensity ratio of 0.20 for the  $\Psi_2$  and  $\Psi_3$  origins requires a vibronic reduction factor of 0.08 to agree with the observed intensity ratio of 0.016. This implies that the reduction factor calculated in the preceding paragraph is far too low. This is most likely due to the overestimation of the displacement of the  $\Psi_2$  potential surface. The broad band centered at 12 130  $cm^{-1}$  also contains the  $\Psi_{x^2-y^2} \rightarrow \Psi_1$  transition (whose zero-phonon line is not observed), which will both broaden and shift to higher energy the apparent Franck-Condon maxima for the  $\Psi_{x^2-y^2} \rightarrow \Psi_2$  transition. This will lead to an overestimate of the  $\Psi_2$  displacement and therefore a lower vibronic reduction factor. In addition these bands are mainly electric dipole in character and the energy difference  $\Delta E$ , in (12), should be between the band maxima and the effective vibronic origin of the transition.

The displacement of the  $\Psi_2$  potential surface required to give a reduction factor of 0.08 necessary for agreement between the observed and calculated  $\Psi_2/\Psi_3$  intensity ratio is  $D = 2.5$ . The analysis is further complicated because the magnetic dipole intensities are also functions of this effective coordinate. However,

the general picture of what is occurring is clear and is shown schematically in Figure 16. The Zeeman experiments have shown that the tetragonal elongation in the  $T_{2g}$  multiplet is less than in the ground state. This fixes the sign of the displacements given in Figure 16.

It is interesting to compare these potential surfaces with that expected for a  $CuF_6^{4-}$  complex in an octahedral environment. In the absence of spin-orbit coupling, the  $E_g \otimes e$  and  $T_{2g} \otimes e$  Jahn-Teller effects would result in the tetragonal distortion of the equilibrium geometries in the order  $\Psi_{z^2}(A_{1g}) < \Psi_1 \approx \Psi_2(E_g) < \Psi_3(B_{2g}) < \Psi_{x^2-y^2}(B_{1g})$  in agreement with Figure 16. However, it has been shown<sup>27</sup> that the inclusion of spin-orbit coupling can quench the  $T_{2g} \otimes e$  Jahn-Teller effect so that the equilibrium geometry for the  $T_{2g}$  multiplet is approximately octahedral. In  $K_2CuF_4$ , however, the "strain" of the crystal lattice plays a dominant role, and our experiments, as summarized in Figure 16, suggest that the equilibrium geometry of the  $T_{2g}$  states is still significantly tetragonally elongated.

Figure 16 also shows that an elongated geometry is particularly favorable for observing the  $\Psi_{x^2-y^2} \rightarrow \Psi_3$  magnetic dipole transition, as it is calculated to be both the most intense transition and to suffer least from vibronic reduction. One can show that for a tetragonally compressed octahedral copper(II) complex, the  $\Psi_{z^2}(\Gamma_6) \rightarrow \Psi_3(\Gamma_7)$ ,  $\Psi_1(\Gamma_6)$  zero-phonon origins are strongly magnetic dipole allowed and have only a small amount of vibronic reduction, as the excited-state minima are almost vertically above the ground-state minimum. Both these transitions for tetragonally compressed copper(II) have recently been observed.<sup>27</sup>

## Conclusions

The optical spectrum of the d-d transitions in the  $K_2CuF_4$  crystal can be understood in terms of tetragonally elongated octahedra with the elongation axes of the two crystal sites being orthogonal to each other within the  $c$  planes. The assignment of these transitions is consistent with AOM bonding parameters and the absorption, MCD, MLD, and ESR spectra. This assignment agrees with that of Reinen et al.<sup>4,7</sup> but differs from that given by other workers.<sup>9-13</sup>

The effective local symmetry at the Cu(II) sites is  $D_{4h}$  and, in contrast to the case of  $KCuF_3$ , the orthorhombic field in  $K_2CuF_4$  is very small. This is consistent with the fact that the bridging fluoride ions will bond more weakly<sup>29</sup> than the terminal fluoride ions with bonds of the same length. This conclusion does not imply that the space group is necessarily tetragonal. However, we find that the vibrations that are strongly coupled to the electronic transitions can be successfully analyzed within the effective  $D_{4h}^5$  space group.

Two magnetic dipole zero-phonon lines have been observed, and their Zeeman splittings confirm the present assignment. The bulk of the observed intensity is due to vibronically induced electric dipole transitions. The vibronic selection rules necessary to interpret the most prominent false origin require the use of the factor group symmetry of the crystal rather than the point group of the isolated complex.

The electronic structure of  $K_2CuF_4$  is characterized by large tetragonal distortions for both the ground and excited electronic states. For the  $T_{2g}$  multiplet this distortion, although smaller than in the ground state, cannot be explained without considering the structure of  $K_2CuF_4$ . A significant portion of the tetragonal distortion of the excited states must be due to the strain generated by the tetragonally distorted lattice.

The study of the electronic properties of  $K_2CuF_4$  is of particular interest in view of the structural relationship it has with the new high-temperature superconductors. The Jahn-Teller effect, intrinsic to a six-coordinate copper(II) complex, is responsible for the orbital ordering that results in the in-plane ferromagnetic exchange interactions in  $K_2CuF_4$ . It has been suggested<sup>42</sup> that the Jahn-Teller effect may also lead to a pairing mechanism in

**Table V.** Zero-Field Energies and Wave Functions from Perturbation Theory

State	Symmetry	Energy/cm <sup>-1</sup> <sup>a</sup>	Wavefunctions <sup>b</sup>
$\Psi_1$	$\Gamma_6$	$-2(\pi_{\parallel} + \pi_{\perp}) + \frac{1}{2}\lambda_{\parallel} + \frac{3}{2}\lambda_{\perp}^2 / [(\sigma_{\perp} + 2\sigma_{\parallel}) - 2(\pi_{\perp} + \pi_{\parallel}) + \frac{1}{2}\lambda_{\parallel}]$	$\Gamma_6(E_g) + a_1\Gamma_6(A_{1g})$
$\Psi_2$	$\Gamma_7$	$E_+ + (c\kappa_{\parallel} + s/\sqrt{2}k_{\perp})^2\lambda_0^2 / [E_+ + 3\sigma_{\perp}]$	$c\Gamma_7(B_{2g}) + s\Gamma_7(E_g) + a_2\Gamma_7(B_{1g})$
$\Psi_3$	$\Gamma_7$	$E_- + (s\kappa_{\parallel} - c/\sqrt{2}k_{\perp})^2\lambda_0^2 / [E_- + 3\sigma_{\perp}]$	$-s\Gamma_7(B_{2g}) + c\Gamma_7(E_g) + a_3\Gamma_7(B_{1g})$
$\Psi_{z^2}$	$\Gamma_6$	$-(\sigma_{\perp} + 2\sigma_{\parallel}) + \frac{3}{2}\lambda_{\perp}^2 / [2(\pi_{\parallel} + \pi_{\perp}) - \frac{1}{2}\lambda_{\parallel} - (\sigma_{\perp} + 2\sigma_{\parallel})]$	$\Gamma_6(A_{1g}) - a_1\Gamma_6(E_g)$
$\Psi_{x^2-y^2}$	$\Gamma_7$	$-3\sigma_{\perp} - (c\lambda_{\parallel} + \sqrt{\frac{3}{2}}s\lambda_{\perp})^2 / [E_+ + 3\sigma_{\perp}] - (s\lambda_{\parallel} - \sqrt{\frac{3}{2}}c\lambda_{\perp})^2 / [E_- + 3\sigma_{\perp}]$	$\Gamma_7(B_{1g}) + (sa_3 - ca_2)\Gamma_7(B_{2g}) - (sa_2 + ca_3)\Gamma_7(E_g)$

$$^a E_{\pm} = -(3\pi_{\perp} + \pi_{\parallel} + \frac{1}{4}\lambda_{\parallel}) \pm \frac{1}{2} [ (2(\pi_{\parallel} - \pi_{\perp}) + \frac{1}{2}\lambda_{\parallel})^2 + 2\lambda_{\perp}^2 ]^{1/2}$$

$$\lambda_{\perp} = k_{\perp}\lambda_0, \lambda_{\parallel} = k_{\parallel}\lambda_0, c = \cos\theta, s = \sin\theta, 2\theta = \tan^{-1} [ 2\sqrt{2}\lambda_{\perp} / (4(\pi_{\parallel} - \pi_{\perp}) + \lambda_{\parallel}) ], 0 \leq 2\theta \leq \pi.$$

$$a_1 = \sqrt{\frac{3}{2}}\lambda_{\perp} / [2\sigma_{\parallel} + \sigma_{\perp} - 2(\pi_{\parallel} + \pi_{\perp}) + \frac{1}{2}\lambda_{\parallel}], a_2 = (c\lambda_{\parallel} + \sqrt{\frac{3}{2}}s\lambda_{\perp}) / [E_+ + 3\sigma_{\perp}], a_3 = -(s\lambda_{\parallel} - \sqrt{\frac{3}{2}}c\lambda_{\perp}) / [E_- + 3\sigma_{\perp}]$$

<sup>b</sup> The wave functions are expressed in terms of the basis functions given in (A1.1).

the high-temperature superconductors.

### Appendix A1. Perturbation Calculations

Spin-orbit coupling and a  $D_{4h}$  ligand field splits the free ion state  $^2D$  of Cu(II) into the  $2\Gamma_6 + 3\Gamma_7$  spin-orbit states. Using the coupling coefficients of Koster et al.,<sup>35</sup> the complex symmetry-adapted wave functions are

$$\begin{aligned}
 ^2E \quad \Gamma_{6\pm}(A_{1g}): & \quad |\pm 1/2 u\rangle \\
 & \quad \Gamma_{7\pm}(B_{1g}): \quad |\pm 1/2 v\rangle \\
 ^2T_2 \quad \Gamma_{6\pm}(E_g): & \quad \sqrt{1/2} [ |i \mp 1/2 \xi\rangle \pm | \mp 1/2 \eta\rangle ] \\
 & \quad \Gamma_{7\pm}(B_{2g}): \quad \mp |i \pm 1/2 \zeta\rangle \\
 & \quad \Gamma_{7\pm}(E_g): \quad \sqrt{1/2} [ |i \mp 1/2 \xi\rangle \mp | \mp 1/2 \eta\rangle ] \quad (A1.1)
 \end{aligned}$$

The  $u, v, \xi, \zeta,$  and  $\eta$  symbols have their usual meanings<sup>28</sup> and represent the antisymmetrized Slater determinantal  $d^9$  functions, e.g.  $|+1/2 u\rangle = |u^+ v^2 \xi^2 \eta^2 \zeta^2\rangle$ . The ligand field and spin-orbit coupling matrix elements have the sign opposite to those in a  $d^1$  basis, while the matrix elements of the Zeeman operator have the same sign.

Below  $T_c = 6.25$  K, the magnetization is described by a molecular field

$$\mathcal{H}_{ex} = 2\mu_B S B_{ex} \quad (A1.2)$$

where  $B_{ex} \approx 30$  T for the ground multiplet and is oriented along four equivalent directions parallel to the crystal  $a$  axes, forming multimagnetic domains. The molecular field is easily rotated by a small external field,<sup>11</sup> and all the MCD and Zeeman experiments as well as the calculated spectra were made under the condition of ferromagnetic saturation along the direction of the applied field. The value of  $B_{ex}$  for the  $^2T_2$  multiplet was treated as a parameter to be determined by fitting the calculated and experimental magneto-optical spectra.

The magneto-optical spectra of the zero-phonon lines were calculated by diagonalizing the  $10 \times 10$  matrix containing the ligand field, spin-orbit, Zeeman, and molecular field matrix elements with (A1.1) as a basis. In all cases we have assumed that  $\Delta_i \approx 1/3\Delta_c$ , a relationship that holds for the ground equilibrium geometry. An artificially small bandwidth was used to reveal the fine structure. The calculated spectra were not sensitive to the value of  $\Delta$ , and the results (Figures 9–13) are displayed as a function of  $\Delta_c$ .

The tetragonal field and spin-orbit coupling energies are much larger than the internal magnetic fields, and we can derive approximate formulas for the  $g$  values and magnetic dipole intensities by neglecting field-dependent admixing of the electronic states. To construct approximate wave functions, the matrix element connecting the  $\Gamma_7(B_{2g})$  and  $\Gamma_7(E_g)$  states was removed by a simple  $2 \times 2$  diagonalization, while the remaining off-diagonal elements

	$ 0_{x^2-y^2}\rangle$	$ 0_{z^2}\rangle$	$ 0_3\rangle$	$ 0_2\rangle$	$ 0_1\rangle$
$\langle 0_{x^2-y^2}  $	$-3\sigma_{\perp}$	0	$-s\lambda_{\parallel} + \frac{c}{\sqrt{2}}\lambda_{\perp}$	$c\lambda_{\perp} + \frac{s}{\sqrt{2}}\lambda_{\perp}$	0
$\langle 0_{z^2}  $	0	$-(\sigma_{\perp} + 2\sigma_{\parallel})$	0	0	$\sqrt{\frac{3}{2}}\lambda_{\perp}$
$\langle 0_3  $	$-s\lambda_{\parallel} + \frac{c}{\sqrt{2}}\lambda_{\perp}$	0	$E_+$	0	0
$\langle 0_2  $	$c\lambda_{\perp} + \frac{s}{\sqrt{2}}\lambda_{\perp}$	0	0	$E_-$	0
$\langle 0_1  $	0	$\sqrt{\frac{3}{2}}\lambda_{\perp}$	0	0	$-2(\pi_{\parallel} + \pi_{\perp}) + \frac{1}{2}\lambda_{\parallel}$

$$E_{\pm} = -3\pi_{\perp} - \pi_{\parallel} - \frac{1}{4}\lambda_{\parallel} \pm \frac{1}{2} [ (2(\pi_{\parallel} - \pi_{\perp}) + \frac{1}{2}\lambda_{\parallel})^2 + 2\lambda_{\perp}^2 ]^{1/2}, c = \cos\theta, s = \sin\theta, 2\theta = \tan^{-1} [ \frac{2\sqrt{2}\lambda_{\perp}}{4(\pi_{\parallel} - \pi_{\perp}) + \lambda_{\parallel}} ], 0 \leq 2\theta < \pi.$$

**Figure 17.** Energy matrix of spin-orbit coupling and tetragonal ligand field potentials for the  $d^9$  configuration. The matrix elements of the Zeeman and molecular field Hamiltonian are omitted for clarity. The cubic anisotropy in spin-orbit coupling is neglected.

**Table VI.**  $g$  Values Obtained from Perturbation Theory

State	$g_{\parallel}^a$	$g_{\perp}$
$\Psi_1$	$g_s(a_1^2 - 1) + 2k_{\parallel}$	$g_s a_1^2 - 2\sqrt{6}a_1 k_{\perp}$
$\Psi_2$	$g_s(a_2^2 - C2\theta) - 2k_{\parallel}(s^2 + 4ca_2)$	$g_s(a_2^2 - c^2) - \sqrt{2}k_{\perp}(2sa_2 - S2\theta)$
$\Psi_3$	$g_s(a_3^2 - C2\theta) - 2k_{\parallel}(c^2 - 4sa_3)$	$g_s(a_3^2 - s^2) - \sqrt{2}k_{\perp}(2ca_3 + S2\theta)$
$\Psi_{z^2}$	$g_s(1 - 3u_{\perp}^2) + 3k_{\parallel}u_{\perp}^2$	$g_s(1 - \frac{3}{2}u_{\perp}^2) + 6k_{\perp}u_{\perp} - 3k_{\parallel}u_{\perp}^2$
$\Psi_{x^2-y^2}$	$g_s(1 - v_{\perp}^2) + 8k_{\parallel}v_{\parallel} - 4k_{\perp}v_{\parallel}v_{\perp} - k_{\parallel}v_{\perp}^2$	$g_s(1 - 2v_{\parallel}^2 - \frac{1}{2}v_{\perp}^2) + 2k_{\perp}v_{\perp} + k_{\parallel}v_{\perp}^2$

<sup>a</sup> The cubic anisotropy in orbital reduction and spin-orbit parameter is ignored. The parameters  $u_{\parallel}$  and  $u_{\perp}$  are defined as  $k_{\parallel}\lambda_0/E(xy \leftarrow z^2)$  and  $k_{\perp}\lambda_0/E(xz, yz \leftarrow z^2)$ , respectively.  $z^2$  is replaced by  $x^2 - y^2$  for  $v_{\parallel}$  and  $v_{\perp}$ , and  $\lambda_i \sim k_i\lambda_0$ . The parameters  $s, c,$  and  $a_i$  are defined in Table V,  $C2\theta = c^2 - s^2$ , and  $S2\theta = 2sc$ .

were treated by perturbation theory. Figure 17 shows the matrix elements of spin-orbit coupling and ligand field potentials. The electronic basis functions,  $\phi$ , are related to the basis of Koster et al.<sup>35</sup> given in (A1.1) by

$$\phi_{x^2-y^2\pm} = \Gamma_{7\pm}(B_{1g})$$

$$\phi_{z^2\pm} = \Gamma_{6\pm}(A_{1g})$$

$$\phi_{3\pm} = (-\sin \theta)\Gamma_{7\pm}(B_{2g}) + (\cos \theta)\Gamma_{7\pm}(E_g)$$

$$\phi_{2\pm} = (\cos \theta)\Gamma_{7\pm}(B_{2g}) + (\sin \theta)\Gamma_{7\pm}(E_g)$$

$$\phi_{1\pm} = \Gamma_{6\pm}(E_g) \quad (A1.3)$$

where  $\theta$  is defined in Figure 17. The matrix is diagonal within the  $e_g$  and  $t_{2g}$  blocks so that, in the case of a strong cubic ligand

**Table VII.** Magnetic Dipole Intensities and MCD Parameters Obtained from Perturbation Theory

Transition <sup>a</sup>	$\alpha, \pi^b$	$\sigma$	$\Delta M^c$	$\Delta M/M$
$\rightarrow \Psi_1$	$I_1^2$	$2 I_1^2$	0	0
$\rightarrow \Psi_2$	$I_2^2 + I_2'^2$	$2 I_2^2$	$2 I_2 I_2'$	$2 I_2 I_2' / (I_2^2 + I_2'^2)$
$\rightarrow \Psi_3$	$I_3^2 + I_3'^2$	$2 I_3^2$	$2 I_3 I_3'$	$2 I_3 I_3' / (I_3^2 + I_3'^2)$
$\Psi_{x^2-y^2} \rightarrow \Psi_{z^2}$	$I_{z^2}^2$	$2 I_{z^2}^2$	0	0

<sup>a</sup>  $I_i$  and  $I_i'$  are the magnetic dipole amplitudes in local x, y and z polarization, respectively.

$$I_1 = -\sqrt{\frac{T}{2}} k_{\perp} (1 - ca_2 + sa_3 - \sqrt{3} a_1 (sa_2 + ca_3)) - \frac{g_s}{2} (sa_2 + ca_3)$$

$$I_2 = -\sqrt{\frac{T}{2}} k_{\perp} (s + 2sca_2 + (c^2 - s^2)a_3 - a_2 (sa_2 + ca_3)) + \frac{g_s}{2} (a_2 (1 + c^2) - sca_3)$$

$$I_3 = -\sqrt{\frac{T}{2}} k_{\perp} (c + (c^2 - s^2)a_2 - 2sca_3 - a_3 (sa_2 + ca_3)) + \frac{g_s}{2} (a_3 (1 + s^2) - sca_2)$$

$$I_2' = -k_{\parallel} (2c - s(sa_2 + ca_3) - 2a_2(ca_2 - sa_3)) + g_s (sa_2 + ca_3)$$

$$I_3' = k_{\parallel} (2s + c(sa_2 + ca_3) - 2a_3(sa_3 - ca_2)) + cg_s (sa_2 + ca_3)$$

$$I_{z^2} = \sqrt{\frac{T}{2}} k_{\perp} (a_1 (1 - ca_2 + sa_3) + \sqrt{3} (sa_2 + ca_3)) + a_1 \frac{g_s}{2} (sa_2 + ca_3) \text{ where } a_i, s \text{ and } c \text{ are given in Table V.}$$

<sup>b</sup> These intensities are for ferromagnetic saturation along the **a** crystal axes and are identical to the case of no magnetic field. <sup>c</sup> Ferromagnetic saturation along the **c** crystal axes, transverse to the elongated molecular axes.

Note that the coefficients  $a_i$  are small, of the order  $\lambda/\Delta$ , and for strong tetragonal fields  $c=0$  and  $s=1$ .

field, perturbation theory will work quite well. The energies correct to second order and eigenstates,  $\Psi$ , correct to first order are given in Table V.

The  $g$  values are defined as<sup>43</sup>

$$g_{\parallel} = 2 \langle \Psi^+ | k_x l_z + g_s s_z | \Psi^+ \rangle$$

$$g_{\perp} = 2 \langle \Psi^+ | k_x l_x + g_s s_x | \Psi^- \rangle \quad (\text{A1.4})$$

The evaluation of (A1.4) with the perturbation wave functions gives the approximate expressions for the  $g$  values in Table VI. Similarly, using (1), (7), and (8), we have calculated the magnetic dipole and the differential circularly polarized magnetic dipole strengths, which are given in Table VII.

#### Appendix A2. Factor Group Analysis

A factor group analysis of the lattice vibrations can be made using either the correlation<sup>44</sup> or the Bhagavantan and Venkatarayudu<sup>45</sup> methods. In the space group  $D_{4h}^2$ , the 39 optical lattice modes due to the 14 atoms in the unit cell transform as the following irreducible representations

$$\Gamma_{\text{Raman}} = 3A_{1g} + B_{1g} + 3B_{2g} + 5E_g$$

$$\Gamma_{\text{IR}} = 3A_{2u} + 7E_u$$

$$\Gamma_{\text{inactive}} = A_{2g} + 4B_{1u} \quad (\text{A2.1})$$

The correlation between the free  $\text{CuF}_6^{4-}$  ion and the site and factor group symmetries is given in Table VIII. The symmetry coordinates that form a basis in each of these irreducible representations can easily be found by using standard methods, and several of the gerade modes are given in ref 15. The modes of  $a_{2u}$  and  $b_{1u}$  symmetry are of special interest here, and the form of these modes has been given in Figure 14. These vibrations correspond to those at the centre of the Brillouin zone ( $k=0$ ), where all the unit cells are vibrating in phase, making it possible to analyze the

**Table VIII.** Correlation between the Vibrational Species for Single-Ion, Site, and Factor Groups

	Single-Ion		Site Group		Factor Group <sup>a</sup>	
	$O_h$	$D_{4h}$	$D_{2h}$	$D_{4h}$	$D_{4h}$	$D_{4h}$
$A_{1g}(s)$	$2A_{1g}$	$B_{1g}$	$3A_g$	$2A_{1g}$	$A_{2g}$	$B_{1g}$
$E_g(s)$	$B_{2g}$	$B_{2g}$	$B_{2g}$	$2B_{2g}$	$2B_{2g}$	$3E_g$
$T_{2g}(b)$	$E_g$	$B_{3g}$	$3B_{1u}$	$2A_{2u}$	$2A_{2u}$	$3B_{1u}$
$2T_{1u}(s,b)$	$2A_{2u}$	$3B_{2u}$	$3B_{3u}$	$3B_{1u}$	$3B_{1u}$	$5E_u$
$T_{2u}(b)$	$B_{2u}$	$3E_u$				

<sup>a</sup> The number of factor group vibrations does not correspond to twice that of the  $\text{CuF}_6^{4-}$  complex since there are only  $2 \times (\text{CuF}_4)$  atoms per Bravais cell corresponding to  $(3N - 3) = 27$  factor group modes involving motion of the Cu and F atoms. The factor group modes involving  $K^+$  ions are  $a_{1g}, b_{2g}, 2e_g, a_{2u}, b_{1u}$ , and  $2e_u$ .

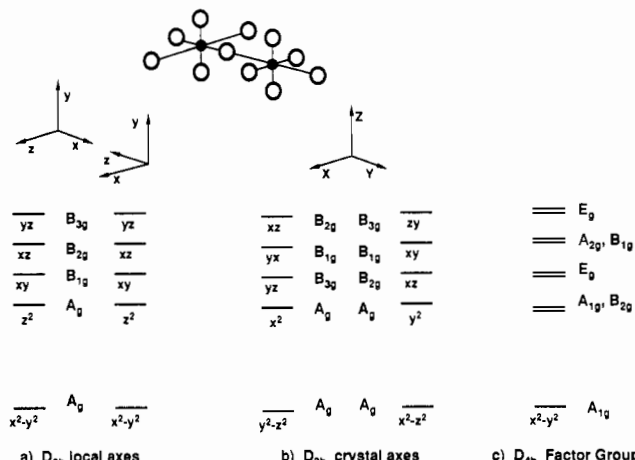


**Figure 18.** Symmetry of the single-ion electronic wave functions in the  $D_{2h}$  point group using (a) the local molecular axes and (b) the crystal axes. The symmetry of the pair electronic wave functions in the  $D_{4h}$  factor group of the crystal is shown in (c).

- (43) Poole, C. P.; Farach, H. A. *The Theory of Magnetic Resonance*; Wiley: New York, 1972.
- (44) Fately, W. G.; Dollish, F. R.; McDevitt, N. T.; Bentley, F. F. *Infrared and Raman Selection Rules for Molecular and Lattice Vibrations: The Correlation Method*; Wiley-Interscience: New York, 1972.
- (45) Bhagavantan, S.; Venkatarayudu, T. *Theory of Groups and their Application to Physical Problems*, 2nd ed.; Bangalore Press: Bangalore City, India, 1951.

crystal vibrations by considering a single unit cell of the crystal.

The classification of the electronic states, in terms of the factor (space) group of the crystal, can also be found by the correlation of Bhagavantam and Venkatarayudu methods.<sup>44</sup> Since the electronic functions can be represented as simple products of single ion electronic states and we are only interested in single excitations,

there will be a one-pair function for the unexcited ground state and eight singly excited pair functions. The correlation between the free  $\text{CuF}_6^{4-}$  ion and the site and factor group symmetries is shown in Figure 18. The four transitions for the free molecule in this orbital basis increases to eight for the two molecules per unit cell.

Contribution from the Department of Chemistry, Stanford University, Stanford, California 94305, and Laboratoire d'Optique Physique, ESPCI, 10 rue Vauquelin, 75231 Paris Cedex 05, France

## Variable-Photon-Energy Photoelectron Spectroscopic Studies of High-Spin $d^6$ Tetrahedral $\text{FeCl}_4^{2-}$ : Electronic Relaxation Effects on Ionization

Kristine D. Butcher,<sup>†</sup> Stephen V. Didziulis,<sup>†</sup> Bernard Briat,<sup>‡</sup> and Edward I. Solomon<sup>\*†</sup>

Received September 20, 1989

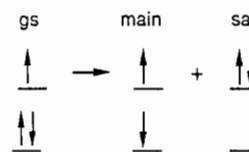
Variable-photon-energy photoelectron spectra (PES) are reported for the valence band region of ferrous chloride over the energy range 25–150 eV. Changes in peak intensity as a function of photon energy are compared to atomic photoionization cross sections, allowing experimental assignment and quantitation of the PES features. These results indicate that the ground-state-bonding description in ferrous chloride corresponds to the normal description for transition-metal complexes, with the highest occupied levels containing mostly metal character, but with significant spin-polarization effects. The relatively large exchange splitting in  $d^6$  splits the  $d$  levels into spin-up and spin-down sets, with the majority spin-up levels showing greater covalent mixing in both the experimental data and in spin-unrestricted SCF- $X\alpha$ -SW calculations. The PE spectra further show satellite peaks with significant off-resonance intensity ( $\sim 6\%$  of the main-band intensity), indicating that a large electronic relaxation occurs upon ionization. PE spectra taken at the Fe 3p absorption edge show dominant resonance enhancement in the deeper binding-energy region of the main band as well as in the satellites. The  $X\alpha$ -SW calculations reproduce both the large relaxation effects and the observed resonance behavior and assign the satellites as arising from ligand ionization plus ligand-to-metal charge-transfer shakeup. The resonance profiles of ferrous chloride are very similar to those of ferric chloride, which shows no relaxation on ionization, but has an inverted energy level description for the majority spin-up levels in the ground state (with the highest occupied orbital containing mostly ligand character). The resonance PES profiles thus indicate that ionized ferrous chloride has relaxed sufficiently to become inverted due to the decrease in electron repulsion and increase in exchange stabilization present in the high-spin  $d^5$  final state. The role of exchange in determining both the ground-state bonding and its change on ionization are considered, and the implications of electronic relaxation for ferrous redox chemistry are discussed.

### I. Introduction

High-spin ferrous complexes play an important role in inorganic redox chemistry, particularly in bioinorganic systems. The single iron-sulfur site in rubredoxin has been the focus of a number of theoretical and spectroscopic studies.<sup>1,2</sup> For the ferrous state, a normal ground-state-bonding description is predicted with the antibonding HOMO containing mostly metal character.<sup>1a</sup> However, calculations on high-spin ferric systems indicate the presence of an inverted ground-state-bonding scheme with the HOMO described as mostly ligand in character.<sup>1c</sup> This inverted ground state has now been demonstrated experimentally in our photoelectron spectroscopic (PES) studies of  $\text{FeCl}_4^-$ , and is due to the large exchange stabilization of the high-spin  $d^5$  configuration.<sup>3</sup> Spin-unrestricted (but not spin-restricted) SCF- $X\alpha$  scattered-wave calculations reproduce our experimental PES data and show that the majority spin (spin-up,  $\uparrow$ ) energy levels (i.e. those having the same spin as the uncompensated valence electrons) are energetically stabilized and have significantly different wave functions relative to their spin-down ( $\downarrow$ ) counterparts. In addition, both the PES data and the  $X\alpha$  calculations show that the ferric system exhibits little change in electronic structure, (i.e. orbital relaxation) upon ionization. These results indicate that a large change in the iron electronic structure occurs upon oxidation. The goal of this study is to use PES to experimentally determine the bonding scheme present in the ferrous tetrachloride ground state and its change upon ionization and to relate this to electronic relaxation contributions to redox processes.<sup>4</sup>

Our previous PES study of  $d^9$   $\text{CuCl}_4^{2-}$  systems demonstrated that dramatic wave function changes can occur upon ionization.<sup>4a</sup> The orbitals relax in order to minimize the large change in metal-centered electron repulsion that can occur upon ionization. As a result of this relaxation, intensity is shifted from the main-band, one-electron PES peaks into deeper binding-energy

### Scheme I



satellite peaks.<sup>5</sup> The satellite peak corresponds to the simultaneous ionization plus shakeup of a second electron to create an excited final state of the complex (Scheme I). This formally two-electron transition is forbidden and should have no intensity. However, final-state relaxation allows the wave functions to change and thus intensity is shifted from the lowest energy final state into the excited (satellite) final state, provided that the shakeup involves an energy level of the same symmetry as the one-electron-ionized final state.<sup>6</sup>

In order to make a detailed assignment and quantitative evaluation of the valence band PES features, we exploit the changes in peak intensity with input photon energy using syn-

- (1) (a) Bair, R. A.; Goddard, W. A., III. *J. Am. Chem. Soc.* **1978**, *100*, 5669. (b) Norman, J. G., Jr.; Ryan, P. B.; Noodleman, L. *J. Am. Chem. Soc.* **1980**, *102*, 4279. (c) Norman, J. G., Jr.; Jackels, S. C. *J. Am. Chem. Soc.* **1975**, *97*, 3833.
- (2) (a) Deaton, J. C.; Gebhard, M. S.; Koch, S. A.; Millar, M.; Solomon, E. I. *J. Am. Chem. Soc.* **1988**, *110*, 6241. (b) Deaton, J. C.; Gebhard, M. S.; Solomon, E. I. *Inorg. Chem.* **1989**, *28*, 877. (c) Gebhard, M. S.; Deaton, J. C.; Koch, S. A.; Millar, M.; Solomon, E. I. *J. Am. Chem. Soc.*, in press.
- (3) Butcher, K. D.; Didziulis, S. V.; Briat, B.; Solomon, E. I. *J. Am. Chem. Soc.*, in press.
- (4) (a) Didziulis, S. V.; Cohen, S. L.; Gewirth, A. A.; Solomon, E. I. *J. Am. Chem. Soc.* **1988**, *110*, 250. (b) Didziulis, S. V.; Cohen, S. L.; Butcher, K. D.; Solomon, E. I. *Inorg. Chem.* **1988**, *27*, 2238.
- (5) (a) Frost, D. C.; Ishitani, A.; McDowell, C. A. *Mol. Phys.* **1972**, *24*, 861. (b) van der Laan, G. *Solid State Commun.* **1982**, *42*, 165. (c) Thuler, M. R.; Benbow, R. L.; Hurych, Z. *Phys. Rev. B: Condens. Matter* **1982**, *26*, 669.
- (6) Manne, R.; Åberg, T. *Chem. Phys. Lett.* **1970**, *7*, 282.

<sup>†</sup>Stanford University.

<sup>‡</sup>ESPCI.